



A Radio, Optical, UV, and X-Ray View of the Enigmatic Changing-look Active Galactic Nucleus 1ES 1927+654 from Its Pre- to Postflare States

Sibasish Laha^{1,2,3} , Eileen Meyer⁴ , Agniva Roychowdhury⁴ , Josefa Becerra Gonzalez^{5,6} , J. A. Acosta-Pulido^{5,6} , Aditya Thapa⁴ , Ritesh Ghosh⁷ , Ehud Behar⁸ , Luigi C. Gallo⁹, Gerard A. Kriss¹⁰ , Francesca Panessa¹¹ , Stefano Bianchi¹² , Fabio La Franca¹² , Nicolas Scepi¹³, Mitchell C. Begelman¹³ , Anna Lia Longinotti¹⁴ , Elisabeta Lusso^{15,16} , Samantha Oates¹⁷ , Matt Nicholl¹⁷ , and S. Bradley Cenko^{2,18}

¹ Center for Space Science and Technology, University of Maryland Baltimore County, 1000 Hilltop Circle, Baltimore, MD 21250, USA; sibasish.laha@nasa.gov

² Astrophysics Science Division, NASA Goddard Space Flight Center, Greenbelt, MD 20771, USA; sib.laha@gmail.com

³ Center for Research and Exploration in Space Science and Technology, NASA/GSFC, Greenbelt, Maryland 20771, USA

⁴ Department of Physics, University of Maryland, Baltimore County, 1000 Hilltop Circle, Baltimore, MD 21250, USA

⁵ Instituto de Astrofísica de Canarias (IAC), E-38200 La Laguna, Tenerife, Spain

⁶ Universidad de La Laguna (ULL), Departamento de Astrofísica, E-38206 La Laguna, Tenerife, Spain

⁷ Inter-University Centre for Astronomy and Astrophysics (IUCAA), Pune, 411007, India

⁸ Department of Physics, Technion, Haifa 32000, Israel

⁹ Department of Astronomy & Physics, Saint Mary's University, 923 Robie Street, Halifax, Nova Scotia, B3H 3C3, Canada

¹⁰ Space Telescope Science Institute, 3700 San Martin Drive, Baltimore, MD 21218, USA

¹¹ INAF—Istituto di Astrofisica e Planetologia Spaziali, via Fosso del Cavaliere 100, I-00133 Roma, Italy

¹² Dipartimento di Matematica e Fisica, Università degli Studi Roma Tre, Via della Vasca Navale 84, I-00146, Roma, Italy

¹³ JILA, University of Colorado and National Institute of Standards and Technology, 440 UCB, Boulder, CO 80309-0440, USA

¹⁴ Instituto de Astronomía, Universidad Nacional Autónoma de México, Circuito Exterior, Ciudad Universitaria, Ciudad de México 04510, México

¹⁵ Dipartimento di Fisica e Astronomia, Università di Firenze, Via G. Sansone 1, I-50019, Sesto Fiorentino, Firenze, Italy

¹⁶ INAF—Osservatorio Astrofisico di Arcetri, Largo Enrico Fermi 5, I-50125, Firenze, Italy

¹⁷ Birmingham Institute for Gravitational Wave Astronomy and School of Physics and Astronomy, University of Birmingham, Birmingham B15 2TT, UK

¹⁸ Joint Space-Science Institute, University of Maryland, College Park, MD 20742, USA

Received 2021 December 16; revised 2022 March 11; accepted 2022 March 31; published 2022 May 18

Abstract

The nearby Type II active galactic nucleus (AGN) 1ES 1927+654 went through a violent changing-look (CL) event beginning 2017 December during which the optical and UV fluxes increased by four magnitudes over a few months, and broad emission lines newly appeared in the optical/UV. By 2018 July, the X-ray coronal emission had completely vanished, only to reappear a few months later. In this work we report the evolution of the radio, optical, UV and X-rays from the preflare state through mid-2021 with new and archival data from the Very Long Baseline Array, the European VLBI Network, the Very Large Array, the Telescopio Nazionale Galileo, Gran Telescopio Canarias, The Neil Gehrels Swift observatory, and XMM-Newton. The main results from our work are (i) the source has returned to its pre-CL state in optical, UV, and X-ray; the disk–corona relation has been reestablished as it has been in the pre-CL state, with an $\alpha_{\text{OX}} \sim 1.02$. The optical spectra are dominated by narrow emission lines. (ii) The UV light curve follows a shallower slope of $\propto t^{-0.91 \pm 0.04}$ compared to that predicted by a tidal disruption event. We conjecture that a magnetic flux inversion event is the possible cause for this enigmatic event. (iii) The compact radio emission which we tracked in the pre-CL (2014), during CL (2018), and post-CL (2021) at spatial scales < 1 pc was at its lowest level during the CL event in 2018, nearly contemporaneous with a low 2–10 keV emission. The radio to X-ray ratio of the compact source $L_{\text{Radio}}/L_{\text{X-ray}} \sim 10^{-5.5}$ follows the Güdel–Benz relation, typically found in coronally active stars and several AGNs. (iv) We do not detect any presence of nascent jets at the spatial scales of ~ 5 –10 pc.

Unified Astronomy Thesaurus concepts: [Active galaxies \(17\)](#)

1. Introduction

The exact geometry and functioning of the central engines of active galactic nuclei (AGNs) are still highly debated. The long duty cycle of AGNs (10^7 – 10^9 yr; Marconi et al. 2004; Schawinski et al. 2015) compared to human timescales is expected to prevent direct observation of the ignition or quenching of an AGN. However, recent discoveries of so-called changing-look AGNs (CL-AGNs) have given us rare glimpses of extreme changes in the AGN state in a few months to years. Not all of these changes happen in the same way, which intimates the complexity of the physical mechanisms at work in the central engine.

CL-AGNs are rare, with only a few dozen candidates in the literature. The term applies both to sources that change from an approximately Type I to Type II state and vice versa. For example, one of the earliest discovered CL-AGNs, Mkn 1018, transitioned from a Seyfert 1.9 to Type 1 over the course of ~ 5 yr in the early 1980s (Cohen et al. 1986). The higher activity state was maintained for decades before significantly dimming (factor of ~ 25) and changing back to Seyfert Type 1.9 during 2013–2015. The X-ray spectra showed no detectable absorption, hence the dramatic change must be intrinsic to the accretion disk emission itself, suggesting major changes in the accretion flow (Husemann et al. 2016).

In contrast, in Mrk 590 (one of the best-observed CL-AGNs) the initially Type 1 source dimmed in the optical by a factor of ~ 100 over three decades, with the complete disappearance of the formerly strong and broad H α emission line (Denney et al. 2014;



Original content from this work may be used under the terms of the [Creative Commons Attribution 4.0 licence](#). Any further distribution of this work must maintain attribution to the author(s) and the title of the work, journal citation and DOI.

Mathur et al. 2018). A prominent soft X-ray excess during the “bright state,” when the broad $H\alpha$ and $H\beta$ lines were present in the optical band, could not be explained by disk reflection. No obscuration in X-rays was detected, but ultrafast outflows and a nascent jet recently discovered with VLBI are present (Yang et al. 2021). It has been suggested that the CL nature of this AGN could be due to episodic accretion events, as it has been observed to rebrighten and dim more than once. A similar case is Mrk 335; originally one of the X-ray-brightest AGNs, the flux dropped dramatically in 2007 (Grupe et al. 2012). Since then, optical, UV, and X-ray monitoring suggest the corona has “collapsed” in toward the black hole (Gallo et al. 2018; Tripathi et al. 2020), and the source sometimes forms a collimated outflow in X-ray flare states (Wilkins et al. 2015; Wilkins & Gallo 2015; Gallo et al. 2019).

The nearby ($z = 0.017$, luminosity distance = 74.2 Mpc) CL-AGN IES 1927+654, the subject of this paper, is a more recent discovery (R.A. = 291.83, decl. = 65.56 in degrees, J2000). It had been previously classified as a true Type II AGN, defying the unification model (Panessa & Bassani 2002; Bianchi et al. 2012), because there had been no detection of broad $H\alpha$ and $H\beta$ emission lines, neither was there any line-of-sight obscuration in the optical, UV or X-rays (Boller et al. 2003; Gallo et al. 2013, and references therein). Tran et al. (2011) suggested that the broad-line region (BLR) is absent due to the low Eddington ratio of this source (i.e., there not being enough continuum emission to light up the BLR). Wang et al. (2012) suggested that the AGN in IES 1927+654 is young and did not have the time to create a BLR.

The dramatic CL event in IES 1927+654 began with a significant rise in the optical/UV in December 2017 (detected by the ATLAS survey; Trakhtenbrot et al. 2019). It continued to rise in luminosity for ~ 150 days, and by the peak in 2018 March, the optical had increased by four magnitudes (almost a factor of 100). Afterwards, the optical/UV decayed with a $t^{-5/3}$ tidal disruption event (TDE)-like light curve (Trakhtenbrot et al. 2019). The optical spectrum just after the flare began was dominated by a blue continuum and several narrow emission lines including $H\alpha$, $H\beta$, and $O[\text{III}] \lambda 5007$, implying that the BLR had not yet responded. The narrow emission lines were consistent with gas photoionized by the AGN continuum (Trakhtenbrot et al. 2019). Strong broad $H\alpha$ and $H\beta$ emission lines (FWHM $\sim 17,000 \text{ km s}^{-1}$) started to appear around ~ 100 days after the flare (between March 6 and April 23 in 2018). The lines remained strong for the next ~ 300 days, after which there was a large Balmer decrement, indicating the presence of dust absorption. The X-ray monitoring of the source started after ~ 100 days of the initial flare, after which the X-ray emission started decreasing rapidly and reached a minimum of 10^{-3} times its original flux in about ~ 200 days after the initial flare. In its lowest flux state, the spectrum shows only soft (0.3–2 keV) emission with no signature from 2 to 10 keV, as expected for coronal emission. This indicates that the X-ray-emitting corona was completely destroyed in the process (Ricci et al. 2021). The X-ray spectrum soon recovered to a flux level of ~ 10 times that of the preflare flux in another 100 days (i.e., by 2019 April).

In this work we investigate the present active state of IES 1927+654, with new observations obtained through 2021. We also utilize archival observations (in all wavelength bands) to better trace the full evolution of this source before, during,

and after the CL event. In this paper, we address in particular the following questions:

1. What is the cause for this violent event? Is it due to the changes in the external rate of mass supply (accretion efficiency due to a TDE) or an internal mechanism related to the change of polarity of the magnetic field of the accretion disk?
2. In the current postflare state, is the X-ray corona fully formed?
3. Is the disk–corona relation established?
4. What is the origin of the soft X-ray emission, which was still sustained when the X-ray corona completely vanished?
5. Is this really a true Type II AGN? What do we infer from the broad-line emission region detection?
6. How has the core ($< 1 \text{ pc}$) radio luminosity evolved during the entire cycle from pre- to postflare states?
7. Are there any indications of nascent jet formation or winds, 3 yr after the flare erupted?

The paper is arranged as follows: Section 2 describes the observation, data reduction techniques, and data analysis of the multiwavelength observations. Section 3 describes the main results from our observational campaigns. This is followed by discussions in Section 4, and conclusions in Section 5. Throughout this paper, we assumed a cosmology with $H_0 = 71 \text{ km s}^{-1} \text{ Mpc}^{-1}$, $\Omega_\Lambda = 0.73$, and $\Omega_M = 0.27$.

2. Observation, Data Reduction, and Data Analysis

2.1. Swift-XRT and UVOT

New observations of IES 1927+654 were carried out by The Neil Gehrels Swift Observatory (from now on Swift) during 2021 at a monthly cadence under a Director’s Discretionary Time (DDT) program (PI: S.Laha), which we present here. We have also analyzed all the archival Swift observations from 2018 and 2019 to make a comparison between the flaring and postflare states. Table 1 lists all the Swift observations, and their short ids (S01–S31). The Swift X-ray Telescope (XRT Burrows; et al. 2005) observations were performed mostly in photon-counting mode, and a few times in window timing mode. We analyzed the XRT data with standard procedures using XRTPIPELINE. The HEASOFT package version 6.28 and the most recent calibration database (CALDB) were used for filtering and screening the data. In the cases taken in photon-counting mode, the source regions were selected using $40''$ circles centered around the centroid of the source, and the background regions were selected with similarly sized circles away from the source. In the observations that were taken in window timing mode, the source and background regions were selected in boxes 40 pixels long. We use the standard grade selections of 0–2 for the window timing mode. Source photons for the light curve and spectra were extracted with XSELECT in both modes. The auxiliary response files (ARFs) were created using the task xrtmkarf and using the response matrices obtained from the latest Swift CALDB. We bin the data using grppha to have at least 20 counts per bin.

The Ultraviolet-Optical Telescope (UVOT; Roming et al. 2005) observed the source IES 1927 in 2018–2019 with all the six filters i.e., in the optical (V , B , U) bands and the near-UV ($W1$, $M2$, $W2$) bands, but only with UVM2 and UVW2 in 2021. Because we are interested in a consistent photometric

Table 1
The Multiwavelength Observations of IES 1927+654

| Observation Band | Telescopes | Observation Date YYYY-MM-DD | Observation ID | Net Exposure (Sec) | Short-id |
|------------------|-----------------------|--------------------------------|----------------|-----------------------|----------|
| X-ray and UV | Swift XRT/UVOT | 2018-5-17 | 00010682001 | 2190 | S01 |
| " | " | 2018-5-31 | 00010682002 | 1781 | S02 |
| " | " | 2018-6-14 | 00010682003 | 2126 | S03 |
| " | " | 2018-7-10 | 00010682004 | 1599 | S04 |
| " | " | 2018-7-24 | 00010682005 | 2302 | S05 |
| " | " | 2018-8-7 | 00010682006 | 2171 | S06 |
| " | " | 2018-8-23 | 00010682007 | 1977 | S07 |
| " | " | 2018-10-3 | 00010682008 | 1252 | S08 |
| " | " | 2018-10-19 | 00010682009 | 966 | S09 |
| " | " | 2018-10-23 | 00010682010 | 1591 | S10 |
| " | " | 2018-11-21 | 00010682011 | 2174 | S11 |
| " | " | 2018-12-6 | 00010682012 | 1568 | S12 |
| " | " | 2018-12-12 | 00010682013 | 1986 | S13 |
| " | " | 2019-3-28 | 00010682014 | 2138 | S14 |
| " | " | 2019-11-2 | 00088914001 | 207 | S14A |
| " | " | 2021-2-24 | 00010682015 | 864 | S15 |
| " | " | 2021-3-9 | 00010682017 | 308 | S17 |
| " | " | 2021-3-10 | 00010682018 | 1004 | S18 |
| " | " | 2021-3-11 | 00010682019 | 1064 | S19 |
| " | " | 2021-3-12 | 00010682020 | 919 | S20 |
| " | " | 2021-3-13 | 00010682021 | 894 | S21 |
| " | " | 2021-4-12 | 00010682023 | 1900 | S23 |
| " | " | 2021-5-18 | 00010682025 | 710 | S25 |
| " | " | 2021-6-17 | 00010682026 | 1513 | S26 |
| " | " | 2021-7-15 | 00010682027 | 527 | S27 |
| " | " | 2021-8-20 | 00010682028 | 1376 | S28 |
| " | " | 2021-10-20 | 00010682029 | 1696 | S29 |
| " | " | 2021-11-20 | 00010682030 | 1556 | S30 |
| " | " | 2021-12-20 | 00010682031 | 1631 | S31 |
| " | XMM-Newton EPIC-pn/OM | 2011-5-20 | 0671860201 | 28649 | X1 |
| Optical | TNG | 2011-6-2 | ... | 1800 | |
| " | GTC | 2021-3-10 | GTC2021-176 | 450 | |
| " | " | 2021-5-4 | " | 450 | |
| Radio | VLA | 1992-1-31 | AS0452 | 210 | |
| " | " | 1998-6-6 | AB0878 | 240 | |
| " | VLBI | 2013-8-10 | EG079A | 5400 | |
| " | " | 2014-3-25 | EG079B | 5400 | |
| " | " | 2018-12-4 | RSY07 | 10800 | |
| " | VLBA | 2021-3-15 | 21A-403 | 12600 | |

Note. TNG = Telescopio Nazionale Galileo, GTC = Gran Telescopio CANARIAS, VLA = Very Large Array, VLBI = Very Large Baseline Interferometer, VLBA = Very Large Baseline Array.

data point in the UV, for comparison over time, we choose to use *UVW2* for all observations, and *UVM2* where *UVW2* is not present. We used the standard UVOT reprocessing methods and calibration database (Breeveld et al. 2011) to obtain the monochromatic flux density in the UV (with a 5'' selection radius) and the corresponding statistical and systematic errors were obtained by the *uvotsource* task. The UV flux densities were corrected for Galactic absorption using the correction magnitude of $A_{\lambda} = 0.690$ obtained from NASA's Extragalactic Database (NED¹⁹).

2.1.1. Swift XRT Spectral Analysis

To fit the Swift XRT 0.3–10 keV spectra, we assumed a simple baseline model of *tbabs*(bbody+powerlaw)*, following the

preflare 2011 spectral modeling (Gallo et al. 2013). The *tbabs* model represents the neutral Galactic absorption, the *bbody* model describes the soft X-ray excess, and the *powerlaw* model describes the inverse-Compton emission from the AGN corona. The poor signal-to-noise data and the low-flux state of the source in most observations did not allow us to use more complex models. See Table 2 for details of the best-fit parameters and the fit statistics (χ^2/χ^2_{ν}) for every observation. We note that in the observations S04, S05, and S06, we do not detect any X-ray photons with XRT, indicating an X-ray low-flux state. In the cases of S04 and S05, we could put upper limits on the fluxes. As we see from the fit statistics in Table 2, in most cases the baseline model gives a satisfactory fit in the 0.3–10 keV band. We also note from Table 2 that the power-law slope has been very steep during the CL phase ($\Gamma \sim 5$), which gradually reached its preflare value of $\Gamma = 2.21$, over a period of ~ 1200 days. We, however, do not have any Swift monitoring data between 2019 December and

¹⁹ <https://ned.ipac.caltech.edu>

Table 2
The Spectral Parameters Obtained Using Swift and XMM-Newton UV and X-Ray Observations of 1ES 1927+654

| ID (MM/YY) | $F_{0.3-2}$ keV ^a | F_{2-10} keV ^a | $F_{1.5-2.5}$ keV ^a | kT (keV) | Γ | UV Filter | UV Flux Density ^b | α_{OX} | χ^2/χ^2_{ν} |
|--------------|------------------------------|-----------------------------|--------------------------------|-----------------|------------------------|-----------|------------------------------|----------------------|-----------------------|
| X1 (05/11) | 9.41 ± 0.66 | 3.92 ± 0.08 | 1.64 ± 0.02 | 0.20 ± 0.01 | $2.21^{+0.02}_{-0.02}$ | UVM2 | 1.34 ± 0.03 | 1.004 | 185/1.37 |
| S01 (05/18) | 26.41 ± 2.12 | 0.06 ± 0.02 | 0.25 ± 0.04 | 0.15 ± 0.01 | $4.94^{+2.48}_{-0.97}$ | UVW2 | 16.17 ± 0.72 | 1.734 | 45/1.02 |
| S02 (05/18) | 8.32 ± 1.33 | 0.04 ± 0.02 | 0.06 ± 0.02 | ... | $4.86^{+0.33}_{-0.30}$ | UVW2 | 14.67 ± 0.67 | 1.955 | 7.10/1.01 |
| S03 (06/18) | 4.21 ± 0.71 | <0.36 | 0.18 ± 0.14 | ... | $3.61^{+0.62}_{-0.60}$ | UVW2 | 13.00 ± 0.59 | 1.752 | 1.76/0.59 |
| S04 (07/18) | ... | ... | ... | ... | ... | UVW2 | 11.30 ± 0.54 | ... | ... |
| S05 (07/18) | <0.393 | <0.14 | <0.10 | ... | ... | UVW2 | 10.74 ± 0.50 | ... | ... |
| S06(08/18) | <1.44 | <0.01 | <0.01 | ... | ... | UVW2 | 10.57 ± 0.48 | ... | ... |
| S07 (08/18) | 5.01 ± 1.12 | <0.12 | 0.09 ± 0.07 | ... | $4.26^{+0.63}_{-0.60}$ | UVW2 | 9.57 ± 0.44 | 1.816 | 3.47/0.87 |
| S08 (10/18) | 24.14 ± 1.66 | 7.17 ± 3.15 | 1.49 ± 0.24 | 0.14 ± 0.01 | $1.40^{+0.87}_{-1.08}$ | UVW2 | 5.67 ± 0.31 | 1.261 | 26.49/0.80 |
| S09 (10/18) | 44.63 ± 2.32 | 8.57 ± 2.00 | 4.92 ± 0.42 | 0.18 ± 0.03 | $2.62^{+0.19}_{-0.23}$ | UVW2 | 9.00 ± 0.48 | 1.139 | 51.14/0.95 |
| S10 (10/18) | 33.10 ± 1.75 | 2.85 ± 1.09 | 1.72 ± 0.30 | 0.14 ± 0.01 | $2.73^{+0.43}_{-0.79}$ | UVW2 | 8.50 ± 0.43 | 1.305 | 33.89/0.68 |
| S11 (11/18) | 32.31 ± 1.92 | 1.05 ± 0.54 | 1.02 ± 0.20 | 0.15 ± 0.01 | $3.29^{+0.43}_{-0.63}$ | UVW2 | 7.96 ± 0.37 | 1.381 | 32.66/0.76 |
| S12 (12/18) | 19.21 ± 1.71 | 0.89 ± 0.27 | 0.85 ± 0.18 | ... | $3.60^{+0.43}_{-0.63}$ | UVW2 | 8.52 ± 0.43 | 1.423 | 25.30/1.15 |
| S13 (12/18) | 40.61 ± 1.98 | 3.28 ± 0.83 | 2.17 ± 0.21 | 0.16 ± 0.01 | $2.70^{+0.27}_{-0.35}$ | UVW2 | 7.95 ± 0.37 | 1.255 | 78.50/1.38 |
| S14 (03/19) | 51.22 ± 1.86 | 9.81 ± 1.35 | 5.41 ± 0.35 | 0.18 ± 0.01 | $2.46^{+0.14}_{-0.16}$ | UVW2 | 6.09 ± 0.30 | 1.058 | 137.88/1.14 |
| S14A (11/19) | 68.91 ± 7.88 | 27.91 ± 6.27 | 12.35 ± 1.52 | ... | $2.42^{+0.15}_{-0.15}$ | UVW2 | 4.39 ± 0.30 | 0.866 | 25.67/1.35 |
| S15 (02/21) | 19.12 ± 2.22 | 3.46 ± 1.22 | 2.12 ± 0.28 | 0.16 ± 0.02 | $2.59^{+0.36}_{-0.51}$ | UVW2 | 2.17 ± 0.13 | 1.042 | 20/0.83 |
| S17 (03/21) | 32.31 ± 5.21 | 1.34 ± 0.72 | 2.01 ± 0.45 | 0.12 ± 0.02 | $1.79^{+0.78}_{-0.91}$ | UVW2 | 2.17 ± 0.19 | 1.051 | 10/1 |
| S18 (03/21) | 24.55 ± 2.45 | 4.78 ± 0.22 | 3.01 ± 0.19 | 0.19 ± 0.04 | $2.68^{+0.23}_{-0.25}$ | UVW2 | 2.28 ± 0.13 | 0.992 | 30/0.88 |
| S19 (03/21) | 25.73 ± 1.86 | 5.37 ± 1.39 | 3.02 ± 0.23 | 0.20 ± 0.04 | $2.52^{+0.28}_{-0.24}$ | UVW2 | 2.30 ± 0.13 | 0.993 | 55/1.34 |
| S20 (03/21) | 20.44 ± 3.21 | 6.02 ± 2.82 | 2.04 ± 0.24 | 0.13 ± 0.02 | $2.09^{+0.76}_{-0.87}$ | UVW2 | 2.17 ± 0.13 | 1.049 | 25/1.19 |
| S21 (03/21) | 32.31 ± 4.23 | 5.24 ± 1.33 | 4.10 ± 0.19 | 0.28 ± 0.09 | $2.84^{+0.26}_{-0.26}$ | UVW2 | 2.04 ± 0.11 | 0.922 | 44/1.13 |
| S23 (04/21) | 20.24 ± 1.12 | 6.32 ± 0.71 | 3.12 ± 0.21 | 0.16 ± 0.03 | $2.35^{+0.16}_{-0.18}$ | UVM2 | 1.94 ± 0.07 | 0.959 | 60/1.15 |
| S25 (05/21) | 23.91 ± 2.91 | 5.23 ± 1.36 | 2.97 ± 0.44 | ... | $2.76^{+0.19}_{-0.18}$ | UVM2 | 1.83 ± 0.09 | 0.958 | 15.70/0.98 |
| S26 (06/21) | 18.21 ± 1.52 | 6.64 ± 1.43 | 2.88 ± 0.29 | 0.18 ± 0.05 | $2.34^{+0.22}_{-0.31}$ | UVM2 | 1.94 ± 0.09 | 0.972 | 57.17/1.43 |
| S27 (07/21) | 19.15 ± 2.41 | 6.09 ± 2.75 | 3.01 ± 0.64 | 0.58 ± 0.03 | $1.62^{+0.71}_{-0.88}$ | UVM2 | 1.94 ± 0.11 | 0.965 | 18.04/1.64 |
| S28 (08/21) | 17.22 ± 1.45 | 5.90 ± 1.02 | 2.78 ± 0.28 | ... | $2.50^{+0.12}_{-0.12}$ | UVW2 | 2.09 ± 0.09 | 0.991 | 20.46/0.76 |
| S29 (10/21) | 9.74 ± 0.85 | 4.42 ± 0.81 | 1.86 ± 0.18 | ... | $2.35^{+0.12}_{-0.12}$ | UVW2 | 2.06 ± 0.09 | 1.055 | 17.68/0.68 |
| S30 (11/21) | 14.04 ± 1.13 | 4.75 ± 0.84 | 2.27 ± 0.23 | ... | $2.52^{+0.12}_{-0.12}$ | UVW2 | 2.04 ± 0.09 | 1.022 | 23.69/0.82 |
| S31 (12/21) | 20.07 ± 1.24 | 5.94 ± 0.81 | 2.99 ± 0.24 | ... | $2.59^{+0.09}_{-0.09}$ | UVW2 | 2.06 ± 0.09 | 0.981 | 47.33/1.01 |

Notes.

^a Flux in units of 10^{-12} erg cm^{-2} s^{-1} .

^b UV flux density in units of 10^{-15} erg cm^{-2} s^{-1} \AA^{-1} $\alpha_{\text{OX}} = -0.385 \log(F_{2 \text{ keV}}/F_{2500 \text{ \AA}})$ The UV flux density was corrected for Galactic absorption using the correction magnitude of $A_{\lambda} = 0.690$ obtained from NED.

2021 February, so we cannot comment on the source spectral and flux state in that time frame. The highest-flux state in the soft and hard X-rays happened in 2019 November, where the fluxes in the soft and hard X-ray bands are ~ 9 times that of their pre-CL value in 2011. In most cases, we do not have a signal to noise at energies >5 keV. However, to be consistent with the literature we quote the fluxes in the 2–10 keV band, which is the flux obtained by extrapolating the model to 10 keV.

The ratio between X-ray and UV, which we refer to as α_{OX} , is calculated from the ratio of the monochromatic fluxes, i.e., $\alpha_{\text{OX}} = -0.385 \log(F_{2 \text{ keV}}/F_{2500 \text{ \AA}})$ (Lusso et al. 2010). This is an important diagnostic parameter to understand if the accretion disk and the X-ray-emitting corona are physically connected. However, we note that we do not have UV fluxes exactly at 2500 \AA . We mostly use UVM2 (1928 \AA) and UVM2 (2246 \AA), and hence we extrapolated the fluxes obtained at these wavelengths to 2500 \AA assuming a flat spectral slope. Our assumption of a flat slope is valid, as we find from Table 2 that in observations S23–S27 where we used UVM2 the flux densities are similar to those of S15–S21 and S28–S29 where we used UVW2. Table 2 lists the α_{OX} values at different epochs of the CL

state. Figure 1 captures the evolution of 0.3–2 keV, 2–10 keV, and 2500 \AA fluxes, along with α_{OX} over a period of ~ 1400 days postflare.

2.2. XMM-Newton EPIC-pn and Optical Monitor

We have analyzed the 2011 XMM-Newton (Jansen et al. 2001) archival observation of the source 1ES 1927+654. The observation was taken during the preflare state of the source (see Table 1 for details). We used the latest XMM-Newton Science Analysis System (SAS v19.0.0) to process the Observation Data Files (ODFs) from all observations. We preferred EPIC-pn (Strüder et al. 2001) over MOS (Turner et al. 2001) due to its better signal to noise ratio. The EVSELECT task was used to select the single and double events for the pn detector. We created light curves from the event files for each observation; to account for the high background flaring, we used a rate cutoff of <0.4 counts s^{-1} . We also checked the pileup using SAS task *epatplot* and found that none of the observations had any significant pileup. Source and background photons were extracted from a circular region of 40'' centered on the source and away from the source

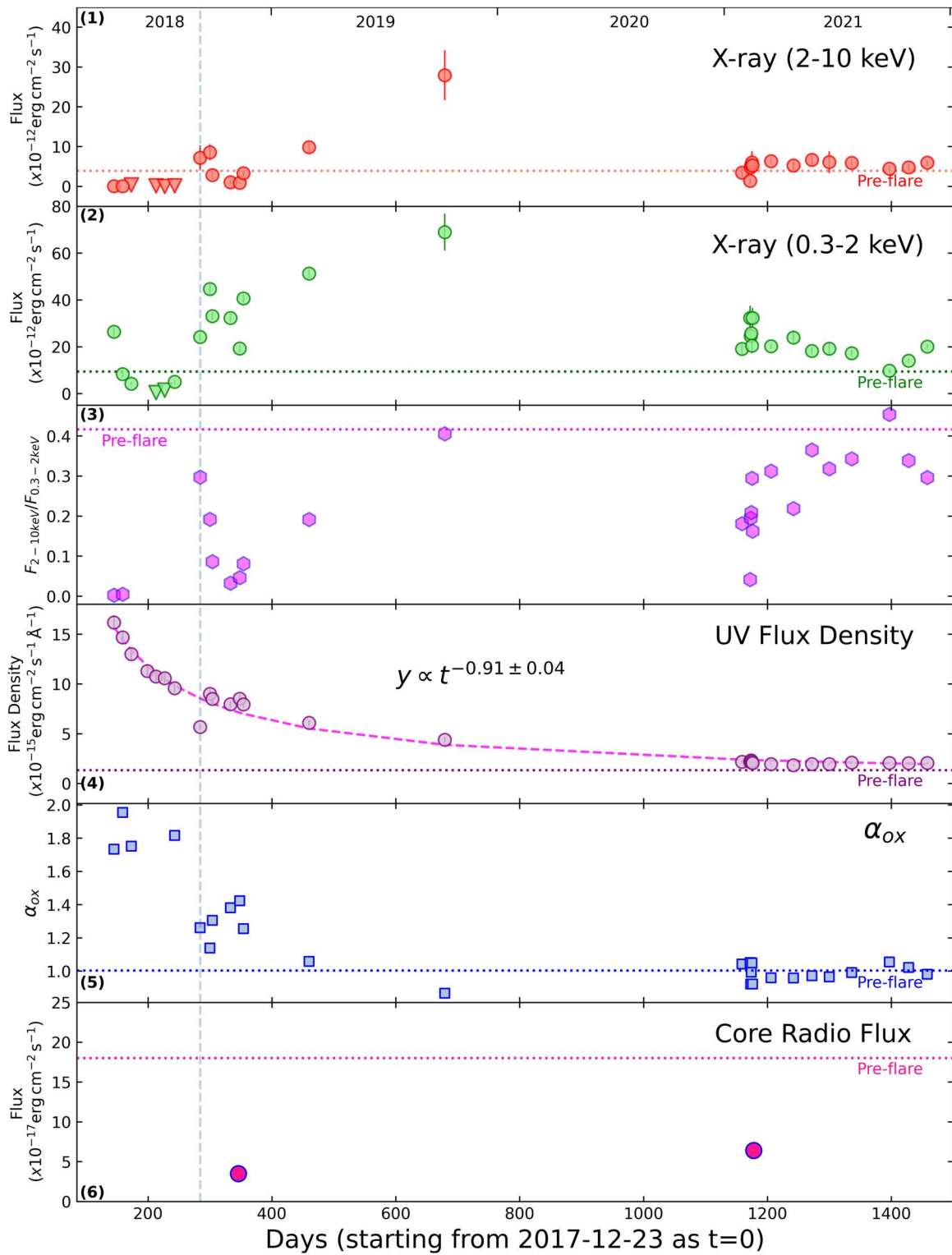


Figure 1. The light curves of the X-ray and UV parameters of the central engine of the AGN 1ES 1927+654, as observed by Swift (see Table 2 for details). The start date of the light curve is 2017 December 23 corresponding to the burst date reported by Trakhtenbrot et al. (2019). The X-axis is in units of days elapsed from the start date. The dotted horizontal lines in every panel refer to their preflare values (in 2011). The inverted triangles are the upper limits. From the top to the bottom panels: (1) The X-ray 2–10 keV flux (in units of $10^{-12} \text{ erg cm}^{-2} \text{ s}^{-1}$), (2) the X-ray 0.3–2 keV flux (in units of $10^{-12} \text{ erg cm}^{-2} \text{ s}^{-1}$), (3) the hardness ratio $F_{2-10 \text{ keV}}/F_{0.3-2 \text{ keV}}$, (4) the UV (UVW2) flux density (in units of $10^{-15} \text{ erg cm}^{-2} \text{ s}^{-1} \text{ \AA}^{-1}$), (5) the α_{OX} , and (6) the core radio flux (<1 pc spatial resolution) Note: The vertical line corresponds to the the observation S8, where the X-ray corona jumps back (created) after being destroyed, and there is a dip in the UV flux by a factor of 2, and also the X-ray spectra become harder (panel 3). There could be a connection between the X-ray corona revival and the dimming of UV emission.

but on the same CCD respectively. The response matrices were generated using the SAS tasks `arfgen` and `rmfgen`. The spectra were grouped using the command `specgroup` with a minimum count of 20 in each energy bin.

The Optical Monitor (OM) (Mason et al. 2001) also collected data during this observations. We did not consider the *V* and *B* bands due to possible host-galaxy contamination and obtained the count rates in four active filters (*U*, UVW1, UVM2, and UVW2) by specifying the R.A. and decl. of the source in the source list file obtained by the OMICHAIN task. In Table 2 we list the UVW2 monochromatic flux densities.

2.2.1. XMM-Newton EPIC-pn Spectral Analysis

The 2011 XMM-Newton observation (preflare) was previously studied by Gallo et al. (2013). The authors found that the source is unobscured ($\leq N_{\text{H}} \sim 10^{20} \text{ cm}^{-2}$) and the X-ray spectrum could be well described by a power law ($\Gamma = 2.27 \pm 0.04$) and a single blackbody component ($kT_{\text{e}} = 170 \pm 5 \text{ eV}$). We followed the similar approach and found best-fit parameter values similar to them ($\Gamma = 2.21 \pm 0.02$ and $kT_{\text{e}} = 200 \pm 10 \text{ eV}$). See Table 2.

2.3. The TNG Optical Observation in 2011

2.3.1. Data Reduction

The pre-CL optical spectrum of 1ES 1927+654 was taken on 2011 June 2 (PI: Panessa), using the DOLORES (Device Optimized for the LOw RESolution) instrument at TNG (Telescopio Nazionale Galileo). Two different gratings have been employed: the low LR-B ($R = 600$ or 460 km s^{-1} around $\text{H}\beta$) and the high VHR-R ($R = 2500$) resolution, with the same $0''.7$ slit. The wavelength range is $3600\text{--}8100 \text{ \AA}$ for the LRB and $6200\text{--}7700 \text{ \AA}$ for the VHR-R. The exposure time was of 300 s and 1500 s, respectively.

The data were reduced using standard processing techniques using MIDAS and IRAF packages. The raw data were bias subtracted and corrected for pixel-to-pixel variations (flat field). Object spectra were extracted and sky subtracted. Cosmic rays were removed. Wavelength calibrations were carried out by comparison with exposures of Ar and Ne+Hg+Kr lamps. Flux calibration was carried out by observations of the spectrophotometric standard star Feige 34 during the same night, with the same instrumental setup, and by correcting for atmospheric extinction.

2.3.2. Stellar Absorption Correction and Emission-line Measurements

We detect significant host-galaxy stellar absorption in the TNG spectrum. The line $\text{H}\beta$ is seen in absorption with a complex profile, formed by a dominant absorption part filled with an emission line. Therefore, in order to properly measure the emission lines, we modeled the stellar population of the host galaxy. We have applied pPXF to fit the stellar population and subtract it to obtain a spectrum containing pure emission lines. During the pPXF process, all the known emission lines are masked to avoid interference with the stellar population determination. Following the host-galaxy stellar absorption subtraction, we modeled the emission-line features using Gaussian components. Several constraints were applied during the fitting process: the line center offsets and relative intensity of the doublets [O III] $\lambda\lambda 4959, 5007$ and [N II] $\lambda\lambda 6548, 6584$ were imposed from the atomic values. The line widths of each

Table 3

Pre-changing-look Optical Spectral Features, Observed in 2011 by TNG

| Line | Wavelength (\AA) | FWHM (km s^{-1}) | Line Flux ($\text{erg cm}^{-2} \text{ s}^{-1}$) ($\times 10^{-15}$) |
|--|--------------------------------|--------------------------------|---|
| $\text{H}\beta$ | 4952.1 ± 0.7 | $555/310 \pm 135$ | 1.25 ± 0.37 |
| [O III]4959 | 5052.45 ± 0.11 | $521/261 \pm 14$ | 2.25 ± 0.08 |
| [O III]5007 | 5101.29 ± 0.11 | $521/268 \pm 14$ | 6.81 ± 0.24 |
| [N II]6548 | 6668.4 ± 1.0 | $417/240 \pm 140$ | 0.51 ± 0.18 |
| $\text{H}\alpha^{\text{a}}$ | 6682.6 ± 0.51 | $721/636 \pm 70$ | 4.09 ± 0.43 |
| [N II]6584 | 6704.4 ± 1.0 | $417/242 \pm 140$ | 1.55 ± 0.53 |
| H α profile modeled by a broad and a narrow component | | | |
| [N II]6548 | 6668.0 ± 0.5 | $421/247 \pm 14$ | 0.43 ± 0.07 |
| $\text{H}\alpha - n^{\text{b}}$ | 6683.0 ± 0.5 | $625/524 \pm 60$ | 3.13 ± 0.49 |
| $\text{H}\alpha - b^{\text{b}}$ | 6673.18 ± 15 | $2644/2621 \pm 700$ | 2.10 ± 1.25 |
| [N II]6584 | 6704.49 ± 0.69 | $421/249 \pm 85.3$ | 1.29 ± 0.22 |

Notes. Measurements of the spectral features in the pre-CL optical spectrum, observed in 2011 by TNG/LRB. The spectrum has been corrected for Galactic extinction. The host-galaxy stellar emission has been subtracted. The two line-width values correspond to the measured/deconvolved by the instrumental profile. The complex $\text{H}\alpha + [\text{N II}]$ has been fitted in two modes: first using a single component for each spectral feature and second using two components for $\text{H}\alpha$, quoted below the horizontal line. In the second mode, the line width for [N II]6548, 6584 was kept fixed to the value obtained in the first case.

^a With a single Gaussian line fit to the $\text{H}\alpha$ complex we found that the line is slightly broad.

^b The $\text{H}\alpha$ emission line was modeled using two Gaussian components for $\text{H}\alpha$: narrow $\text{H}\alpha - n$ and broad $\text{H}\alpha - b$. In this case, the line width of [N II] 6548, 6584 was fixed to the value obtained with a single component.

doublet were also tied to have the same velocity width. The results are presented in Table 3 and Figure 2, left panel.

2.3.3. Fitting the Broad $\text{H}\alpha$ Emission Line

The source had been classically referred to as a true Type II AGN due to its lack of any broad emission-line signature in the optical spectra, as well as lack of any line-of-sight obscuration (Gallo et al. 2013). However, interestingly this source exhibited a transient broad-line region during the CL event (Trakhtenbrot et al. 2019), indicating the presence of a BLR, which is probably not visible due to its low emissivity in normal times. Following this, we carefully searched for the signature/hint of any weak broad line in the 2011 pre-CL TNG spectrum, which could tell us that the BLR existed all through the spectrum but was not bright enough to be seen. After correcting for the host-galaxy stellar absorption, we found that most emission lines exhibit narrow profiles with $\text{FWHM} \leq 500 \text{ km s}^{-1}$ (See Table 3). However, we found some broad positive residuals in the region around the $\text{H}\alpha$ region after we have accounted for the narrow emission lines.

To further investigate the broad residuals, we used an additional broad Gaussian (FWHM and normalization free to vary) over and above the narrow Gaussian used for the $\text{H}\alpha$ profile. We detected a statistically significant improvement in the fit and detected a weak broad $\text{H}\alpha$ emission-line profile with $\text{FWHM} = 2621 \pm 700 \text{ km s}^{-1}$ and line flux of $(2.10 \pm 1.25) \times 10^{-15} \text{ erg cm}^{-2} \text{ s}^{-1}$. See Table 3. A close-up for the most complex emission-line fits, $\text{H}\beta$ and $\text{H}\alpha$, can be found in Figure A3.

Table 4
The Post-changing-look Optical Spectral Features Observed by GTC/OSIRIS in 2021

| Line ID | Center (Å) | FWHM (km s ⁻¹) | Line Flux (erg cm ⁻² s ⁻¹) × 10 ⁻¹⁵ | Comment ^a |
|--------------|----------------|----------------------------|---|----------------------|
| [O II] 3727 | 3796.8 ± 0.6 | 710/285 ± 100 | 2.34 ± 0.4 | new line |
| He II 4686 | 4775.1 ± 0.4 | 795/603 ± 80 | 0.99 ± 0.11 | new line |
| Hβ | 4953.3 ± 0.4 | 660/435 ± 30 | 1.43 ± 0.08 | same |
| [O III] 4959 | 5052.09 ± 0.03 | 505/125 ± 4 | 1.95 ± 0.02 | lower (-15%) |
| [O III] 5007 | 5100.92 ± 0.03 | 505/143 ± 4 | 5.91 ± 0.06 | lower (-13%) |
| [O I] 6300 | 6417.56 ± 0.82 | 477/281 ± 86 | 0.29 ± 0.07 | new line |
| [N II] 6548 | 6670.00 ± 0.19 | 500/335 ± 22 | 0.66 ± 0.04 | higher (+22%) |
| Hα | 6686.22 ± 0.08 | 544/400 ± 9 | 5.64 ± 0.13 | higher (+18%) |
| [N II] 6584 | 6706.06 ± 0.20 | 500/352 ± 22 | 2.00 ± 0.11 | higher (+22%) |

Note. The post-CL optical spectral features measured from the combined spectrum after stellar template subtraction. The spectrum has been corrected for Galactic extinction. The center and width of the lines [O III] 4959, 5007 Å and [N II] 6548, 6584 Å are tied. The line flux ratios [O III] 5007/4959 and [N II] 6584/6548 are kept fixed to the theoretical value of 3.

^a Listing the instances when the lines in the post-CL (2021) spectra have lower, higher, or similar fluxes compared to the pre-CL spectra (2011) reported in Table 3. The two line-width values correspond to those measured/deconvolved by the instrumental line profile.

was taken on 1992 January 31 and consists of one 3.5 minute scan. Standard calibration was applied with source 1959+650 serving as the initial amplitude and phase calibrator and 3C 48 as flux calibrator. Imaging deconvolution was conducted using the task `clean` as implemented in CASA, with a Briggs weighting and robust parameter of 0.5. One round each of phase-only and amplitude and phase self-calibration was applied. The resulting image has an rms of 1.25×10^{-4} Jy beam⁻¹ and the synthesized beam is $4''.51 \times 1''.48$. The radio emission at the C band is unresolved (i.e., a point source); a Gaussian fit to the central peak gives a flux of 16.4 ± 0.2 mJy at a central frequency of 4.86 GHz, in agreement with the value of 16 ± 2 mJy previously published in Perlman et al. (1996).

The X-band observation was taken on 1998 June 6 and consists of two 2 minute scans. The same procedure was followed as for the C band, with source 1800+784 serving as the initial phase calibrator. The final image has an rms of 9.26×10^{-5} Jy beam⁻¹ and synthesized beam of $0''.47 \times 0''.22$. The source is not resolved, and the limits on the source size from the Gaussian fit tool in CASA is less than 88×30 mas, or 34×12 pc. The peak flux of the point source is 9.12 ± 0.11 mJy at a central frequency of 8.46 GHz.

2.6. VLBA

IES 1927+6547 was observed by the Very Long Baseline Array, concurrent with the Swift campaign, on 2021 March 15 under Director’s Discretionary Time proposal 21A-403 (PI: E. Meyer). A standard dual-polarization 6 cm frequency setup was used, with central channel frequencies of 4868, 4900, 4932, 4964, 4996, 5028, 5060, and 5092 MHz and a total bandwidth of 32 MHz. As the source was expected to be too faint for self-calibration, we used a relatively fast-switching cadence between the target and a bright calibrator source, J1933+6540, 1.2 distant. Target scans were 190 s with 30 s on the calibrator. We observed J2005+7752 and J1740+5211 as amplitude check sources. The entire observation was 3.5 hr, resulting in acceptable UV coverage for imaging.

The data were checked for radio frequency interference and then calibrated using the rPicard pipeline (Janssen et al. 2019) installed in Common Astronomy Software Applications (CASA) version 5.6.0. Initial imaging deconvolution was

Clean I map. Array: BFHKL MNOPS
B1927+6527 at 4.980 GHz 2021 Mar 15

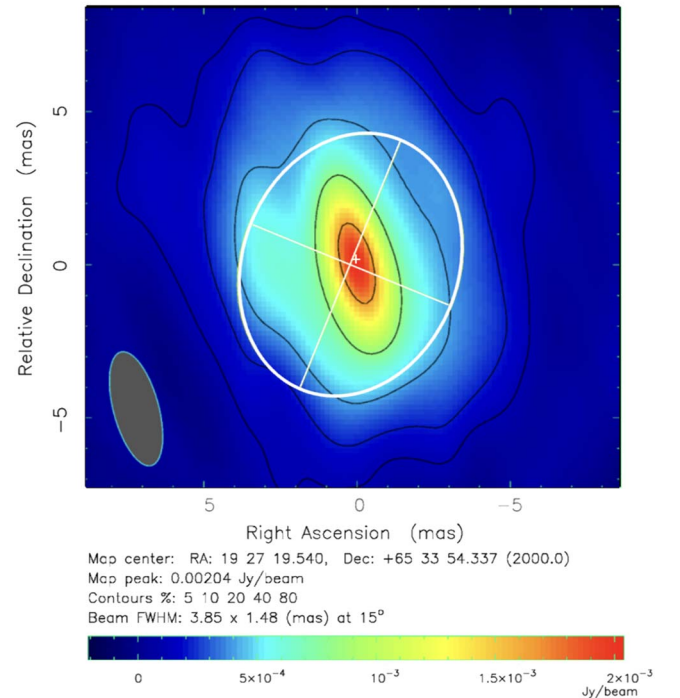


Figure 3. Image corresponding to the 2021 VLBA observation of IES 1927+654, at 4.9 GHz. Extended diffuse emission, in addition to a bright core, is evident. The best-fit point-source+disk model has been illustrated with the point source shown as a small white cross while the disk as the white oval with corresponding major and minor axes. The contours have been plotted as 5%, 10%, 20%, 40%, and 80% of the peak flux. The extended disk model cannot be convolved with the synthesized beam inside DIFMAP and hence this CLEAN map is only the core+residual.

accomplished in DIFMAP (Shepherd et al. 1994) with a map size of 1024 pixels at 0.16 mas pixel⁻¹. The restored image shown in Figure 3 used natural weighting and has an rms sensitivity of $0.5 \mu\text{Jy beam}^{-1}$ and synthesized beam (resolution) of 3.85×1.48 mas. The imaging shows a central peak of approximately 2 mJy beam⁻¹. The total flux is 5.5 ± 0.5 mJy, suggesting a resolved component, and extended emission

around the point source is also apparent in the residual imaging. To determine better the true source structure we used a custom version of DIFMAP `modelfit` (`ngDIFMAP`; A. Roychowdhury et al. 2022, in preparation) to fit the visibilities of the calibrated data with several alternative models including a single unresolved point source and either adding a Gaussian or a uniform disk model to the same. The best model (as determined by the reduced chi-squared) is a point source of 1.4 mJy centered on a uniformly bright disk of 4.1 mJy and size 4.4×3.5 mas, corresponding to 1.8 by 1.4 pc (see Table 6). We used Monte Carlo simulations (e.g., Briggs 1995; Chael et al. 2018; A. Roychowdhury et al. 2022, in preparation) to verify that the extended emission around the point source (shown as a small cross in Figure 3) is intrinsic to the source and is not an artifact of interferometric errors or gaps in $u-v$ coverage.

2.7. EVN

1ES 1927+6547 has been observed by the European VLBI Network (EVN) under project EG079 in 2013 March and 2014 October at 1.5 and 5 GHz respectively, and under project RSY07 in 2018 December at 5 GHz. These epochs will be referred to by year (2013, 2014, and 2018) in the rest of the paper. We note that the first two observations predate the CL event while the 2018 observation was about 1 yr after the optical/UV peak. We used the publicly available pipeline-reduced `uvfits` files²¹ for our analysis. The source was observed for $\sim 3-4$ hr for each of the EVN observations, similar to the VLBA 2021 observation, implying expected sensitivities²² $\sim 10-20 \mu\text{Jy beam}^{-1}$ for all the VLBI data. However, $\sim 3-4$ antennas dropped out for each of the EVN observations, which worsened $u-v$ coverage, and therefore sensitivity.

We used DIFMAP for initial imaging deconvolution with a map size of 1024 pixels at $0.1 \text{ mas pixel}^{-1}$. Using the same modified DIFMAP fitting methods as for the 2021 VLBA observation, we again evaluated alternative models for the radio emission. The best-fit model in both 2013 (1.5 GHz) and 2014 (5 GHz) is an unresolved point source, while the postflare 2018 epoch is better described by a point source atop a uniformly bright disk, as in the 2021 VLBA observation. The best-fit model fluxes, the rms sensitivity, and the resolution (synthesized beam size) have been tabulated in Table 6 along with all other radio observations described here. As noted, the fit results from 2018 and 2021 are similar. Because the EVN data suffered from poorer $u-v$ coverage due to several unusable antennas, we have carefully evaluated the uncertainties in the model parameters through Monte Carlo simulations of the visibilities (A. Roychowdhury et al. 2022, in preparation). For the EVN observations we further assume a minimum 10% error on the flux due to uncertainties in the flux calibration.

3. Results

In this section we present the observational results from our multiwavelength campaign of the CL-AGN 1ES 1927+654. We have used X-ray and UV observations from Swift and XMM-Newton; radio observations from VLA, EVN, and VLBA; and optical observations from the TNG and GTC.

3.1. The X-Ray and UV Spectra and Light Curves

3.1.1. The UV Light Curve

The UV flux density starts off from a high-flux state in 2018 May and drops monotonically until 2021 February (we do not have any observations from 2020), after which it plateaus at a value of $\sim (2.06 \pm 0.11) \times 10^{-15} \text{ erg cm}^{-2} \text{ s}^{-1} \text{ \AA}^{-1}$, its current postflare quiescent state. Table 2 shows that this value is still slightly larger than the pre-CL value of $1.34 \pm 0.03 \times 10^{-15} \text{ erg cm}^{-2} \text{ s}^{-1} \text{ \AA}^{-1}$. From Figure 1 panel 4 we find that the UV light curve drops at a rate $\propto t^{-0.91 \pm 0.04}$, which is a shallower slope than predicted by a TDE event, which is typically $\propto t^{-5/3}$ (van Velzen et al. 2021).

In order to robustly test if the measured slope is indeed shallower, we did the following tests. We fitted a simple exponential function $y = A \times (t - t_0)^b$ to the UV light curve and used the least-squares minimization technique to obtain the best fit, using the Python function `scipy.optimize.curve_fit`. This function returns the best-fit parameters and one standard deviation error on the parameters. For $t_0 = 0$ (i.e., a start date on 2017 December 23), this results in a best-fit slope of $b = -0.91 \pm 0.04$ and a normalization of $A = (1.42 \pm 0.30) \times 10^{-12}$ (see Figure 4). As a next step, we froze the exponent value to that expected for a TDE (that is, $b = -5/3$) and estimated the best fit by allowing the normalization A to vary and for the different cases of the start date t_0 , given that there is some doubt about which day the flare happened. We found that in all cases it did not describe the observed light curve at all (See Figure 4 left panel). The black solid curve on the same figure is the best fit with $b = -0.91 \pm 0.04$. Figure 4, right panel, shows the different fitted curve for different start dates, where both the slope b and normalization A are left free to vary. Even with a spread of start date of ~ 20 days around the time we assumed (2017 December 23), the best-fit slopes are still consistent with $b \sim -0.9$.

3.1.2. The X-Ray Light Curve

The X-rays, however, behave in a completely different manner, as also reported in the previous studies (Ricci et al. 2020, 2021), where the flux drops to a minimum in 2018 June–August (~ 200 days after the start of the flare) and then ramps up from 2018 October until it reaches its highest state in 2019 November (about 10 times its pre-CL value) and then falls back to its pre-CL state. The hard X-rays and soft X-rays do not show any correlated variability. See Figure 5. We note that in the current postflare state (2021) there is still some variability (\sim factor of 2) in both the soft and hard X-ray emission. For example, the soft X-ray emission dropped exactly to its pre-CL value as late as 2021 October, that is, after ~ 1400 days from the start of the flare (see Figure 1, panel 2). The 2–10 keV flux has reached its pre-CL state earlier. From Table 2 we find that for all the X-ray observations, the soft X-ray (0.3–2 keV) flux dominates the overall X-ray luminosity. We also note that the spectra became very soft during the lowest flux states in 2018 (observations S01 to S07), consistent with what has been reported by previous studies (Ricci et al. 2020, 2021).

Figure 1, panel 3, shows the hardness ratio ($\text{HR} = F_{2-10 \text{ keV}}/F_{0.3-2 \text{ keV}}$) light curve during and post-CL event. It is interesting to note that the HR does not follow the trend of the soft or hard X-ray fluxes. The HR reached its pre-CL state in 2019 December, but again dropped to its minimum value in 2021 February. The HR gradually revived to normal pre-CL

²¹ archive.jive.nl/scripts/avo/fitsfinder.php

²² <http://old.evlbi.org/cgi-bin/EVNcalc>

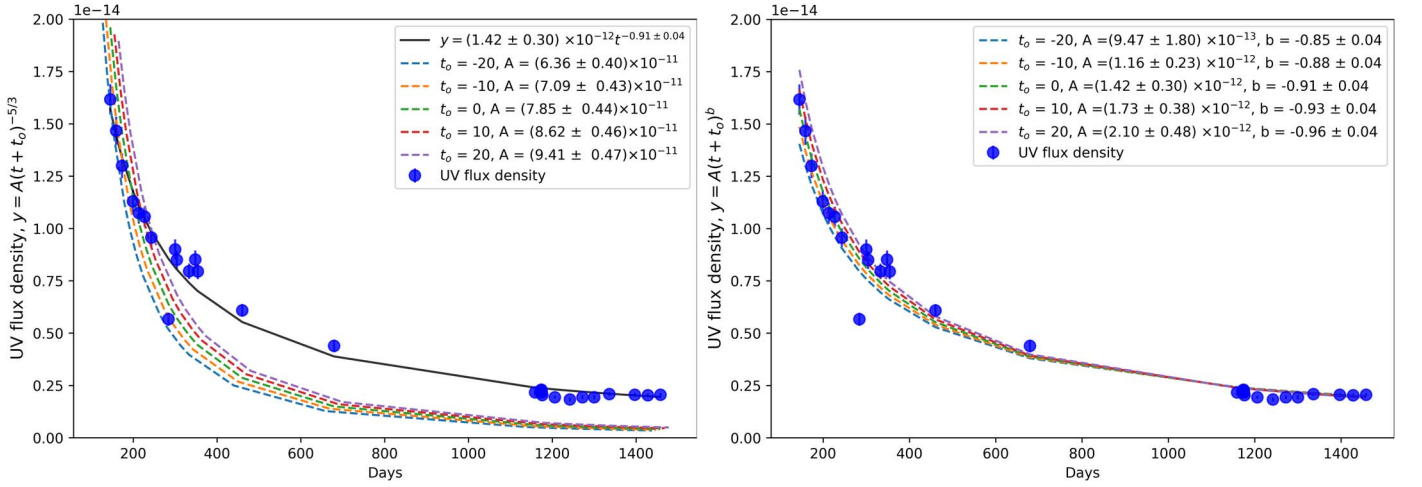


Figure 4. Left: the black curve represents the best fit to the UV flux density, with the equation $y = A \times (t + t_0)^b$, where the starting time $t_0 = 0$ is assumed to be 2017 December 23 following Trakhtenbrot et al. (2019). The blue points are the measured UV flux density (see Table 2). The best-fit values are $A = (1.42 \pm 0.30) \times 10^{-12}$ and $b = -0.91 \pm 0.04$, for $t_0 = 0$. The colored dotted curves are the fits obtained when we froze $b = -5/3$ following the predictions of a TDE. We allowed the normalization A to vary, however, none of them gave a good description of the observed data. Due to the uncertainty in accurately knowing the day of the flare, we have fitted the data with different values of $t_0 = -20, -10, 0, 10$, and 20 , corresponding to 10 and 20 days around 2017 December 23 (different colors). The fitted normalization A in each case is reported in the figure. Right: fitting the UV light curve with the equation $y = A \times (t + t_0)^b$. In this case both A and b are kept free. The best-fit A and the corresponding b values are reported in the figure.

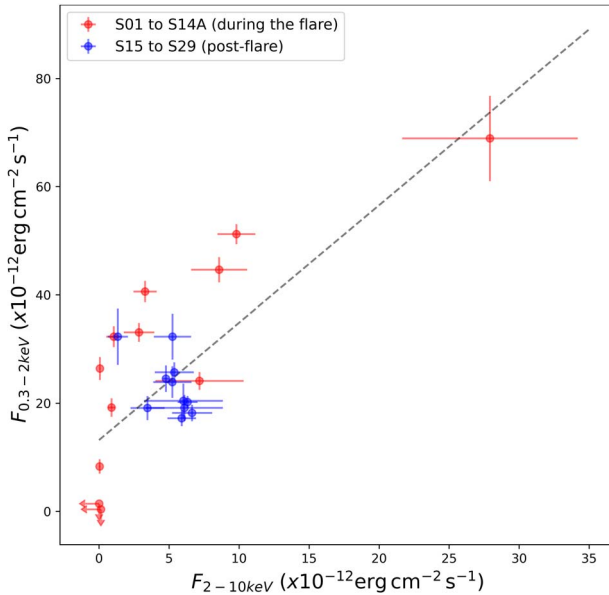


Figure 5. The relation between the soft X-ray (0.3–2 keV) and hard X-ray (2–10 keV) fluxes at different epochs during and after the X-ray flaring period. The red circles denote the X-ray flaring period covering 2018–2019 (observations S01–S14A), while the blue circles denote the postflare period covering 2021 February–October (observations S15–S29). The lowest state in X-rays is denoted by upper limits in both axes in the lower-left corner of the figure. It is clear that the soft and hard X-rays do not show any significant correlation (Spearman rank correlation coefficient = 0.48, with a probability of rejecting the null hypothesis = 98%).

state again in 2021 October. These point to fact that the coronal and the soft X-ray emission are still in a phase of building up.

Another interesting note is that the UV flux drops by a factor of 2 (from its normal falloff) during observation S8, coinciding exactly with the revival of the X-ray coronal emission after the violent event (plotted as a vertical dotted line in Figure 1). We find that the spectra become hard at that point (panel 3) for the first time after days of nondetection of hard X-rays. In Table 2,

we find that we could obtain only upper limits in the 2–10 keV X-ray flux from S03 to S07 observations, and the hard X-ray emission revived in S8.

3.1.3. The Relation between α_{OX} and $L_{2500 \text{ \AA}}$

The universal relation between AGN accretion disk and corona is well described by the strong correlation found between α_{OX} versus $L_{2500 \text{ \AA}}$, across large ranges of black hole mass, accretion rates, and redshift (Lusso et al. 2010). Figure 6 shows the α_{OX} versus $L_{2500 \text{ \AA}}$ for all the Swift observations reported in Table 2. The red star in the lower-left corner of the figure represents the pre-CL value, and interestingly, it is slightly below the Lusso et al. (2010) correlation (red line) indicating a dominant X-ray emission, relative to UV. The other data points obtained during the CL event are scattered all over the phase space indicating that the disk–corona relation was not valid during this violent event. The recent observation data points (S25–S29) are clustered in the lower-left corner (near the red star) of Figure 6, left panel, indicating that the disk–corona relation is gradually being established.

3.2. The Optical Spectra

3.2.1. Comparing the Pre- and Post-changing-look Spectra

In order to check carefully any changes that may have been detected in the pre-CL and post-CL optical spectra, we carried out a uniform analysis for both the 2011 TNG and 2021 GTC spectra. See Figure 2, left and right panels (also the Appendix). We find that the 2011 TNG pre-CL optical spectrum shows a stronger blue continuum than that of the GTC/OSIRIS spectrum. Nevertheless, the emission-line features mostly look similar in both spectra, except for differences in line strength in most of the emission lines (see Tables 3 and 4). We see significant differences in [O III] doublets. We also detect a He II emission line in the 2021 GTC spectra, which was not present in 2011. Both the pre-CL and post-CL spectra show strong intrinsic host-galaxy absorption, which we have carefully and

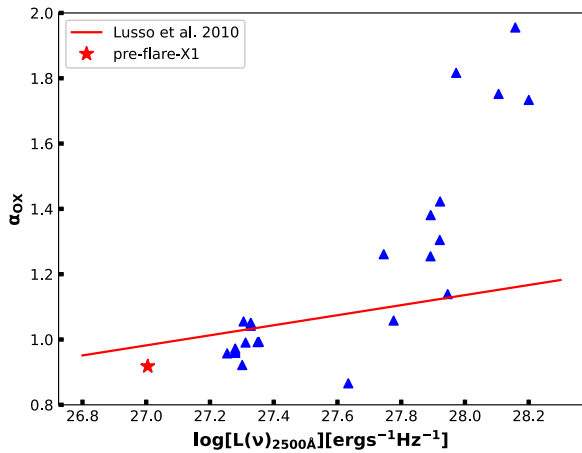


Figure 6. The α_{OX} vs. $L_{2500 \text{ \AA}}$ for the different Swift observations of the source IES 1927+654 as reported in Table 2. The red line denotes the best-fit correlation obtained from Lusso et al. (2010), which denotes the standard AGN disk–corona relation. The red star denotes the 2011 pre-CL state of IES 1927+654.

Table 5
The Optical Diagnostic Emission-line Ratios

| Line Ratio | 2011 | 2021 |
|--------------------------------|--|-------------------|
| $\text{H}\alpha/\text{H}\beta$ | 3.3 ± 1.15 | 3.94 ± 0.3 |
| $[\text{O II}]/\text{H}\beta$ | ... | 1.6 ± 0.3 |
| $[\text{O III}]/\text{H}\beta$ | 5.47 ± 1.8 | 4.14 ± 0.2 |
| $[\text{O I}]/\text{H}\alpha$ | ... | 0.051 ± 0.012 |
| $[\text{N II}]/\text{H}\alpha$ | $0.38 \pm 0.13/0.25 \pm 0.08^{\text{a}}$ | 0.36 ± 0.02 |

Notes. Line ratios are computed after stellar contribution has been subtracted. Note that in either 2011 or 2021, the $\text{H}\beta$ emission line was not detectable unless we subtracted the underlying stellar absorption.

^a Line fluxes were computed assuming a broad component for $\text{H}\alpha$ as described in previous sections.

uniformly modeled. This indicates a host stellar population dominated by young stars. We refer the reader to Table 4, last column, for the changes in the line fluxes relative to the pre-CL state.

3.2.2. The Broad $\text{H}\alpha$ Line in the 2011 Spectrum

We detect a weak broad $\text{H}\alpha$ emission line in the pre-CL TNG spectrum of 2011, with an FWHM of $2600 \pm 700 \text{ km s}^{-1}$ and line normalization of $(2.10 \pm 1.25) \times 10^{-15} \text{ erg cm}^{-2} \text{ s}^{-1}$ (see Table 3 and Figure A3). We applied a likelihood ratio test and found that this broad emission-line component is robustly required by the data. We do not detect any broad emission line in the 2021 GTC spectrum.

3.2.3. Diagnostic Line Ratios

The line ratios $[\text{O III}]/\text{H}\beta$ can be computed only after stellar emission subtraction, because we detect $\text{H}\beta$ in absorption, which pops up as an emission line after host stellar absorption correction. The line ratios $[\text{O III}]/\text{H}\beta$ and $[\text{N II}]/\text{H}\alpha$ derived after stellar template subtraction are also compatible, within the errors, for the two epochs (see Table 5). Note that before stellar template subtraction $[\text{N II}]/\text{H}\alpha$ is higher in the 2011 spectrum compared to the 2021, which can be explained by the decrease in emission flux due to larger stellar contribution in 2011. The

values of the diagnostic line ratios of IES 1927+654 lies in the border line between AGN and starburst galaxies (Kewley et al. 2006). The line ratio $\text{H}\alpha/\text{H}\beta$ is slightly larger than that expected for an AGN (which is ~ 3.1) and may indicate some host intrinsic reddening affecting the narrow-line region. Thus the results indicate that IES 1927+654 lies in the frontier between Seyfert and starburst galaxies.

3.3. Arcsecond- and Milliarcsecond-scale Radio Observations

In the radio regime we were able to cover the preflaring state, in 2013 October and 2014 March, and the postflaring activity in late 2018 and 2021. Table 6 summarizes the low- and high-resolution radio observations of IES 1927+654 currently available with VLA and VLBA. The VLA observations from 1992 and 1998 predate the CL event and provide a useful baseline for comparison to the later and higher-resolution VLBI data. The radio spectral index between the C- and X-band VLA observations is $\alpha_r = -1.1$, a relatively steep value but not unusual for radio-quiet AGNs (Barvainis et al. 2005), especially considering the time baseline and high likelihood of variability.

In all epochs we find an unresolved “point source” component, with a size $< 0.5\text{--}1 \text{ pc}$. The three repeated observations at 5 GHz show that the radio emission is variable: It drops four-fold from 2014 March to 2018 December, and has increased again in 2021 March. This behavior is roughly concurrent with the X-ray flux (see Figure 1, panel 6), and we shall discuss this further in the next section. In both postflare high spatial resolution radio observations (2018 and 2021) we detect a resolved/extended component, which accounts for most of the observed flux.

The extended emission is not detected in the 1.5 GHz 2013 October EVN observation, likely due to the larger synthesized beam. It is also undetected at the higher-resolution 5 GHz EVN observation in 2014 March. We further discuss the interpretation of these results in Sections 4.2 and 4.7.

4. Discussion

IES 1927 has been a unique AGN that is traditionally classified as a true Type II AGN, implying that there has been no detection of broad $\text{H}\alpha$ and $\text{H}\beta$ emission lines, as well as no line-of-sight obscuration in the optical, UV, or X-rays (Boller et al. 2003; Gallo et al. 2013, and references therein). The most important point in the unification theory is that all AGNs have a BLR, and when we do not detect any BLR it means that our line of sight to the central regions is intercepted by an optically thick torus. This notion has already been challenged by this source by not having any BLR. In an interesting turn of events, this source flared up in UV/optical in 2017 December (detected by ATLAS survey; Trakhtenbrot et al. 2019) by four magnitudes in just a matter of weeks and a “transient” BLR (FWHM $\sim 17,000 \text{ km s}^{-1}$) appeared only after ~ 150 days, which gradually vanished over a period of $\sim 1 \text{ yr}$. This proved that the BLR is present but the central source in its normal state is not luminous enough to light it up. The other interesting highlights from the violent CL phase are (1) the UV/optical flare happened in 2017 December, which gradually decreased. (2) A large Balmer decrement happened about $\sim 100\text{--}200$ days after the flare indicating the presence of dust along the line of sight. (3) The corona completely vanished in 2018 August and again came back to normalcy but did not follow the pattern of

Table 6
Details of the Radio Observations, with Corresponding Flux Density Measurements

| Obs. | Freq. (GHz) | Date (MM/YY) | Total Flux (mJy/beam) | Central PS Flux (mJy) | Extended Flux (mJy) | Disk Dimensions (mas × mas) | rms (Jy/beam) | Resolution (mas × mas) | T_B ($\times 10^6$ K) |
|------|-------------|--------------|-----------------------|-----------------------|---------------------|----------------------------------|----------------------|------------------------|--------------------------|
| VLA | 8.46 | 06/98 | 9.0 ± 0.1 | ... | ... | ... | 1.3×10^{-4} | 470×220 | ... |
| VLA | 4.86 | 01/92 | 16.4 ± 0.2 | ... | ... | ... | 9.3×10^{-5} | 4510×1480 | ... |
| EVN | 4.99 | 03/14 | 4.1 ± 0.4 | ... | ... | ... | 3.2×10^{-5} | 2.47×1.18 | 15.0 ± 1.5 |
| EVN | 4.99 | 12/18 | 8.4 ± 0.8 | 0.8 ± 0.1 | 7.6 ± 0.7 | $4.9 \pm 0.9 \times 4.6 \pm 0.5$ | 3.6×10^{-5} | 6.01×4.95 | 0.50 ± 0.05 |
| VLBA | 4.98 | 03/21 | 5.5 ± 0.5 | 1.4 ± 0.1 | 4.1 ± 0.4 | $4.4 \pm 0.1 \times 3.5 \pm 0.1$ | 5.2×10^{-5} | 3.85×1.48 | 5.7 ± 0.6 |
| EVN | 1.48 | 08/13 | 18.9 ± 0.2 | ... | ... | ... | 2.5×10^{-4} | 28.2×11.7 | ... |

Note. In cases where only an unresolved core is observed, the total flux density equals the core flux density. For cases where we detect resolved extended emission, the central point source (PS) flux is noted alongside the extended flux density and the semimajor and semiminor axes of a best-fitting uniform disk model. Note that “flux” in the table headers refers to flux density. The brightness temperature T_B has been calculated for the point source at 5 GHz.

the UV/optical flare, implying that the standard disk–corona relations did not hold during the violent event. In this work, we investigate the pre- to post-CL state of the central engine using multiwavelength observations. Below we discuss different science questions in relation to the results found in this work. Note that the ratio of the core radio to X-ray fluxes of this AGN at different epochs are shown in Figure 7.

4.1. What Caused this Event: Is it a TDE or Magnetic Flux Inversion?

Although the initial papers (Trakhtenbrot et al. 2019; Ricci et al. 2020) reporting this unique event suspected a TDE as the source of the CL event, there were already some concerns. For example, Trakhtenbrot et al. (2019) reported that they did not detect the emission lines in the optical spectra that one would normally detect for a TDE. Similarly Ricci et al. (2020) mentioned that although the UV flux dropped monotonically after the flare, the X-ray flux showed an entirely different behavior, which is not what one would expect from a TDE. For the first time in this work we report that the source is back to its normal state and obtain a light curve in UV and X-rays spanning over 3 yr. We could fit the UV light curve with an exponential function and found that the slope is much shallower $\propto t^{-0.91 \pm 0.04}$, pointing to the fact that it could be something other than a TDE, which may have triggered the event. We, however, cannot rule out the TDE scenario from the shallow slope because it is not clear how a TDE in a preexisting accretion disk would behave (Chan et al. 2019). In a sample of 39 TDEs, van Velzen et al. (2021) found that the median power-law index is $b = -1.6$, which is consistent with the value $b = -5/3$, which one expects for the full disruption of a star.

In any case, given that (1) the UV slope is $\propto t^{-0.91 \pm 0.04}$, (2) the X-ray showed completely uncorrelated behavior in the entire duration of the CL event, (3) the hard X-ray completely vanished after 200 days of the flare, and (4) everything is back to normal in ~ 1400 days, we wanted to test an alternative hypothesis, namely the “magnetic flux inversion” scenario presented in Scepi et al. (2021), in which the mass accretion rate and the magnetic flux on the black hole are the two independent parameters controlling the evolution of the CL event.

Ricci et al. (2020) suggested that the optical CL and the X-ray luminosity variations of 1ES 1927+654 can be explained by a TDE that has destroyed the inner accretion disk, and hence the corona. However, we note that the UV luminosity has monotonically decreased since the flare, yet the X-ray

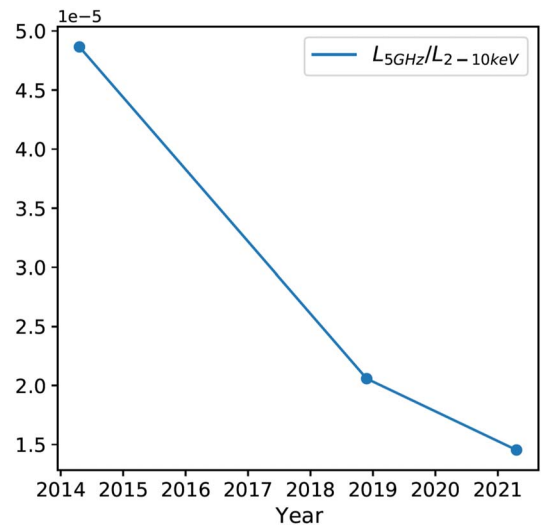


Figure 7. The light curve of the ratio of the 5 GHz monochromatic core radio luminosity with the 2–10 keV luminosity, popularly known as the Güdel–Benz relation. See Table 7 for details.

luminosity was unchanged initially for 100 days, and then it started to fall until it reached a minimum after 200 days of the flare (see Figure 1, panels 1 and 2) when the X-ray coronal emission completely vanished for a period of 2 months (see Table 2). The coronal emission revived in 2018 October, following which the spectra started to become hard. Thus, the optical CL event and the X-ray luminosity are completely uncorrelated. In most cases of “typical CL-AGNs” the X-ray luminosity follows the UV, such as those found in SDSS J015957.64+003310.5 (LaMassa et al. 2015), Mrk 1018 (Husemann et al. 2016), NGC 1566 (Parker et al. 2019), and HE 1136–2304 (Zetzl et al. 2018).

The uncorrelated evolution of the optical/UV and X-ray suggests that two separate physical parameters are changing during this event. Following Scepi et al. (2021), we suggest that the optical/UV are related to a change in the mass accretion rate at some large radii, $\dot{M}(r_{\text{opt}})$, and that the X-rays come from very close to the black hole and are related to a change in the magnetic flux onto the black hole, Φ_{BH} . In a magnetically arrested disk (MAD), Φ_{BH} is proportional to the square root of \dot{M}_{BH} , the accretion rate on the black hole. Hence, the optical/UV and the X-rays should be correlated but with a delay, Δt_{delay} , corresponding to the time it takes for an increase in the accretion rate in the disk to propagate onto the black hole (see blue solid line and red dashed line on Figure 8). However,

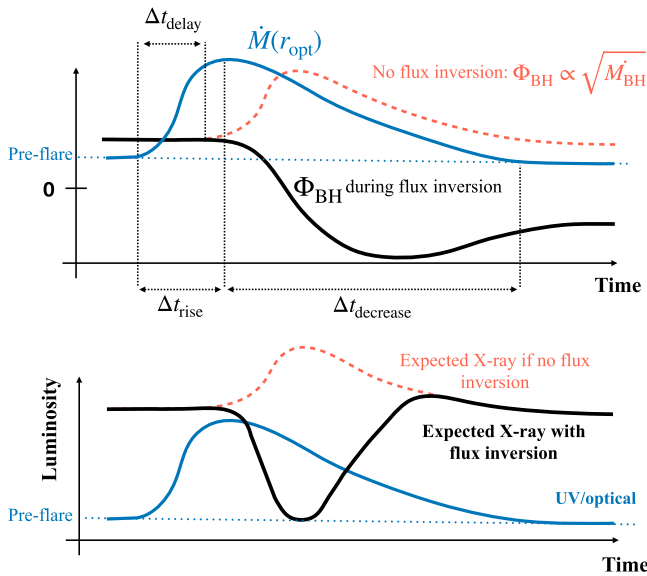


Figure 8. Schematic diagram explaining how a flux inversion event leading to the destruction and regeneration of a magnetically arrested disk (MAD) can explain the separate evolution of the X-rays and the UV of IES 1927+654. Top panel: physical parameters controlling the evolution of the CL-AGN. The mass accretion rate passing through the disk at the optical-UV emission radius, $\dot{M}(r_{\text{opt}})$, is shown as a solid blue line and the magnetic flux on the black hole, Φ_{BH} , in the case of no flux inversion and in the case of a flux inversion are shown respectively as a red dashed line and a solid black line. Bottom panel: dependence of the X-ray and UV luminosities on the physical parameters shown on the top panel. The UV luminosity follows \dot{M} while the X-ray luminosity follows the absolute value of the magnetic flux on the black hole. There is a delay, noted Δt_{delay} , between the evolution in the UV and the evolution in the X-ray due to the time it takes for a change in the disk to propagate to the black hole. During the flux inversion event the X-ray luminosity goes to zero despite the increase of the accretion rate onto the black hole. When the MAD gets regenerated the X-ray luminosity again follows the trend of the accretion rate onto the black hole, and so of the optical/UV.

if the magnetic flux brought in by the disk suddenly changed polarity that would destroy this correlation and suddenly shut off the source of X-rays (see black solid line on Figure 8). Thanks to our new observations, we are now able to further constrain this scenario. Figure 9 shows a cartoon depiction of the magnetic flux inversion event. We note below the most important information that can be extracted from these archival and new observations:

1. The fact that the X-ray and UV luminosities go back to their initial values after the whole event suggests that the CL event is not triggered by a change in mass supply from the environment. The return to the preflare state seems more consistent with an internal mechanism related to the change of polarity. This is reminiscent of Dexter et al. (2014), where the authors observed an increase in \dot{M} during a flux inversion event in their simulation.
2. In the flux inversion scenario, the X-rays always lag the optical/UV by Δt_{delay} , which corresponds to the time for any change in the disk to reach the black hole (see Figure 8). We can measure this delay by the time it takes for the X-rays to show a change once the optical/UV CL event has started. We estimate that $\Delta t_{\text{delay}} \approx 150$ days from the data of Trakhtenbrot et al. (2019), Ricci et al. (2020), and Figure 1.
3. The evolution of the X-rays is complicated because it depends on two parameters, the mass accretion rate \dot{M}_{BH}

and the magnetic flux Φ_{BH} . \dot{M}_{BH} should follow the trend of the optical/UV with a delay of $\Delta t_{\text{delay}} \approx 150$ days as stated above. This means that \dot{M}_{BH} and the X-ray luminosity should reach their maximum value around August of 2018. However, this is right during the dip in the X-rays (Figure 1, panel 1). In our scenario, the reason why the X-rays do not reach a maximum in 2018 August is because the magnetic flux on the black hole is canceled by the advection of magnetic flux of opposite polarity brought along with the increased accretion rate. This destroys the X-ray corona, which is powered by strong magnetic flux near the black hole and so makes the X-rays drop in spite of \dot{M}_{BH} going up. However, after the magnetic flux on the black hole has built up again, recreating the X-ray corona, the X-rays should follow \dot{M}_{BH} again. We believe that this happens somewhere around 2019 November where the X-rays are at their maximum (see Figure 1).

4. After 2019 November, the X-rays and the UV are completely correlated again but with a delay of ≈ 150 days. The fact that the X-rays overshoot their preflare value in 2019 November by a factor of ≈ 6 is marginally consistent with the fact that the UV overshoots its preflare value by a factor of ≈ 3 in 2019 April (the closest observation to 150 days before 2019 November) as expected in the flux inversion scenario.
5. Again, after 2019 November, the X-rays follow the optical/UV with a lag of ≈ 150 days. This means that the X-rays should go down to their preflare value ≈ 150 days after the optical/UV. This is consistent with what is observed as the soft X-rays going back to their preflare value with a delay of ≈ 200 days compared to the optical/UV, as can be seen on Figure 1. We note that the duration of the entire event, meaning the time between the departure from preflare value and the return to preflare value, is the same for the optical/UV and X-rays and is roughly ≈ 1200 days. This is again consistent with the idea that the changes in the optical/UV and X-ray are due to the same event with, however, the X-rays behaving differently because of their dependence on the magnetic flux on the black hole.
6. The time it takes for the optical/UV to rise is $\Delta t_{\text{rise}} \approx 200$ days. This time interval corresponds to the time it takes for the inversion event to leave the region of the disk peaking in the optical/UV. It then provides information on the physical size of the inversion event. Moreover, we see that Δt_{rise} is roughly equal to Δt_{delay} , the time it takes for the inversion event to go from the radius where the disk peaks in the optical/UV to the black hole. This means that the physical size of the inversion event, Δr , is $\approx r$. In other words, the inversion profile is very gradual. This would explain why such an inversion event could have been preserved in the disk without reconnecting before being able to propagate inwards.
7. The radio flux decreases at the same time as the X-ray luminosity drops by three orders of magnitude. In Scepi et al. (2021), we argued that the X-rays should arise from synchrotron emission of high-energy electrons in a corona or failed jet near the black hole. The electrons would also emit synchrotron radiation in radio and so the coincident decrease of the radio and X-rays is consistent with the flux inversion scenario.

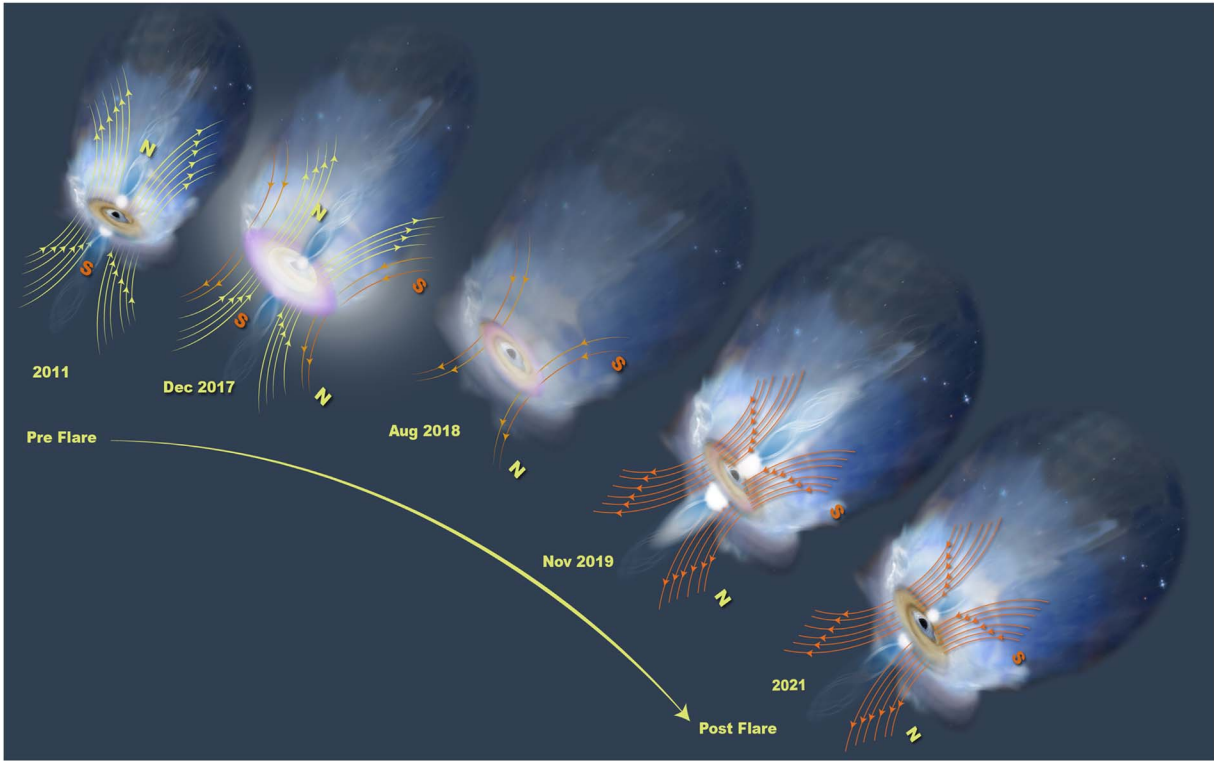


Figure 9. Cartoon representing the magnetic flux inversion event. From left to right are the preflare to postflare states of the central engine. The initial direction of the magnetic field is depicted by yellow lines, while the reversed polarity is shown by red lines. We discuss the individual panels here, 2011: the preflare state of the AGN where the polarity of the magnetic field threading the accretion disk is in one direction. 2017 December: the violent CL event happens, with the accretion disk brightening up by four magnitudes. This is due to an increase in the accretion rate, possibly related to the change of magnetic polarity in the disk shown in red lines. 2018 August: the magnetic flux on the black hole is canceled by the advection of magnetic flux of opposite polarity and hence the corona vanishes. Note that the accretion disk has dimmed from the 2017 state. 2019 November: The magnetic field with reversed polarity now gains strength and hence the corona is revived. Note that the intensity of the corona is several factors larger than that in 2011 because the accretion rate is larger than in its preflare state value as can be seen by looking at the UV disk emission. The accretion disk still continues to dim. 2021: the present-day scenario, where the magnetic field with reversed polarity has fully formed and the corona and the disk have been restored to their preflare 2011 state. Note that the polarity of the magnetic field is opposite that of 2011.

4.2. The Coronal Evolution: A Radio and X-Ray Perspective

The case of the CL-AGN 1ES 1927+654 serves as a curious test bed to investigate the origin of the coronal emission. For the first time in an AGN, the corona completely vanished and then again reappeared in a timescale of ~ 1 yr. A similar phenomenon (contracting corona) has been reported in one of the Galactic black hole binaries (Kara et al. 2019), but never in an AGN. It is evident that the mechanisms that are creating and supplying energy to the X-ray corona must be in a stable equilibrium configuration. That is why it could jump back in a year timescale after being completely destroyed. X-ray and radio observations provide unique insight into the coronal physics. Variations of a few 10% of the radio emission are typically observed in AGNs (Mundell et al. 2009). The radio emission in this source is consistent with the one observed in radio-quiet AGNs (Panessa et al. 2019). We note the following points in this context:

1. The central emission radio peak in the AGN 1ES 1927+654 comes from a region < 0.5 – 1 pc, while the extended emission covers a region of 4 – 10 pc. The observed radio properties are consistent with being produced in the inner region of a low-power jet or a wind or the X-ray-emitting corona.
2. A correlation is found between the core radio (L_R) and X-ray (L_X) luminosities of Radio Quiet (RQ) AGNs in the Palomar-Green sample (Laor & Behar 2008), which follows the relation $L_R/L_X \simeq 10^{-5}$, remarkably similar to

Table 7
Semicontemporaneous X-Ray and Radio Fluxes (Either from 1.5 or 5 GHz VLBI) and the Güdel–Benz Relation

| X-Ray Epoch (MM/YY) | Mean 2–10 keV X-Ray Flux (F_X) ($\text{erg cm}^{-2} \text{s}^{-1}$) | VLBI epoch (MM/YY) | VLBI Flux (F_R) ($\text{erg cm}^{-2} \text{s}^{-1}$) | F_R/F_X |
|---------------------|---|--------------------|--|-----------------------|
| ^a 05/11 | 3.7×10^{-12} | 08/13 | 5×10^{-16} | 1.35×10^{-4} |
| ^a 05/11 | 3.7×10^{-12} | 03/14 | 1.8×10^{-16} | 4.8×10^{-5} |
| 12/18 | 1.7×10^{-12} | 12/18 | 3.5×10^{-17} | 2.0×10^{-5} |
| 03/21 | 4.4×10^{-12} | 03/21 | 6.4×10^{-17} | 1.4×10^{-5} |

Note.

^a There are no contemporaneous X-ray observations of this source along with VLBI in 2013 and 2014. Hence, we used the 2–10 keV flux from the 2011 XMM-Newton observations by Gallo et al. (2013).

the Güdel–Benz relation for coronally active stars (Güdel & Benz 1993). Although the observed radio cores were on scales of few 100 c, radio variability constraints on RQ AGNs have indicated that most of the emission arises from ~ 10 pc-scale compact regions (e.g., Barvainis et al. 2005; Mundell et al. 2009). This is an indication that the radio emission may originate from the corona. Using the radio and X-ray luminosities of the compact core of 1ES 1927+654, we find that $L_R/L_X \sim 10^{-5}$, as illustrated in Table 7 and Figure 7. This is an indication that the

compact radio emission is related to the region from where the X-ray emission is coming, which can possibly be the corona (Laor & Behar 2008).

3. Another interesting aspect is the radio and X-ray light curve. Figure 1, panel 6, shows that the core radio flux decreased by a factor of ~ 4 in 2018 December from its preflare state in 2014, just when the X-ray emission was also at its minimum (~ 2018 August–October). The radio flux has since then picked up but not yet reached its preflare value. The correlated decrease and then increase of the radio flux with the X-ray flux is likely a sign of the coronal recovery and thereafter a coronal (synchrotron) origin of the radio emission.
4. The radio brightness temperatures of the AGN 1ES 1927+654 $T_B \gtrsim 10^6$ K in the preflare and the postflare states (See Table 6 last column) point to a nonthermal origin of the core radio emission. This could either arise from the X-ray corona or a jet knot (Panessa et al. 2022).
5. The steep radio spectrum ($\alpha_r = -1.1$) is consistent with an optically thick regime. In the case of an optically thick synchrotron source, as per Equation (19) in Laor & Behar (2008), the estimated emission region would be ~ 0.001 pc, which is again consistent with the X-ray corona or a very nascent jet.

Given all the evidence, we can say that the core radio emission arises from the innermost regions of the AGN and can possibly be related to the X-ray corona or a nascent unresolved jet.

4.3. The Origin of the Soft X-Ray Emission

The origin of the soft X-ray emission in AGNs is still debated. Popular theories suggest that it could arise out of thermal Comptonization of the UV seed photons by a warm corona (Done et al. 2012) or it can also arise out of the reflection of hard X-ray photons from the corona off the accretion disk (García et al. 2014). Even after a considerable number of studies on the subject (Laha et al. 2011, 2013, 2014a; Ehler et al. 2018; García et al. 2019; Laha et al. 2019; Tripathi et al. 2019; Waddell et al. 2019; Ghosh & Laha 2020; Laha et al. 2020; Ursini et al. 2020; Laha & Ghosh 2021), there has not been a consensus on the physics of the origin of the soft X-ray excess. X-ray reverberation lead/lag studies too have yielded conflicting results for different sources (Kara et al. 2016). Hence, the special cases of CL-AGNs give us a unique platform to investigate the origin of this feature, which is ubiquitously present in bright AGNs. For example in the CL-AGN Mrk 590, it has been seen that the soft X-ray flux remains bright even when the power-law flux goes through a dim state (Mathur et al. 2018), indicating that possibly the soft excess in this source may not arise out of disk reflection of the hard X-ray photons.

The source 1ES 1927+654 has exhibited a strong soft excess at energies below ~ 2 keV in its pre-CL state in 2011, which could be well modeled by a blackbody of $kT = 0.20 \pm 0.01$ keV (See Table 2). Ricci et al. (2021) modeled the XMM-Newton X-ray spectra with complex disk-reflection models but could not obtain a reasonable fit. From Figure 5 we note that the soft and the hard X-ray show no correlated behavior, whether during the X-ray flare (red points) or in the postflare states (blue points). Ricci et al. (2021) using high-cadence NICER observations reports that at around ~ 200 days after the UV flare, the hard X-ray completely vanished (2018 August) for around ~ 3 months

until it reemerged in 2018 October. During this time, the soft X-ray was still present, but in a low state. From these evidences, we can rule out a disk-reflection origin of the soft excess for this source because in the reflection scenario, the hard-X-ray-emitting power law is the primary emitter.

Also, there is no correlation between the UV flux and the soft X-ray flux during and after the CL event, implying the possibility that the origin of the soft excess may not be from the warm Comptonization of the disk UV photons. However, as a caveat, we must note that during the flaring event, the disk was possibly destroyed, and hence, we do not expect standard models to hold.

The other interesting observational points to note in this context for this source are:

1. There is no detection of a narrow or broad FeK α emission line at 6.4 keV (Gallo et al. 2013), which is otherwise commonly detected in most AGNs. This indicates a complex reflection geometry of the central engine.
2. There is a detection of a narrow emission line at 1 keV in the XMM-Newton spectra in the postflare scenario (Ricci et al. 2021). This emission line was not present in 2011 XMM-Newton spectrum.
3. The hardness ratio (HR) plot shows a weird variability pattern. See Figure 1, panel 3. During the hard X-ray dip (~ 200 days after the onset of the flare), the HR is very low (coincident with the vanishing of the corona) and it jumps back in 2018 October, goes down again, and then gradually reaches the pre-CL state over a period of ~ 300 days. We note that even though the HR has reached its pre-CL value, both the soft and the hard X-ray fluxes were almost ~ 8 times higher than their original pre-CL values (See Figure 1). More intriguingly, in 2021 February, when we started monitoring the source with Swift, the HR was again as low as the lowest HR state, and then again climbed up to its pre-CL value over a period of ~ 200 days. These point toward a complex relation between the emitters of soft and hard X-rays. A time-dependent physical modeling can reveal the nature of the soft X-ray emitter.
4. The hard X-ray flux jumps back in 2018 October after staying undetected for ~ 3 months (from 2018 July–October), and at the same time, there is a factor of 2 decrease in the UV luminosity, a quite distinct deviation from its normal $t^{-0.91}$ exponential drop. See Figure 1, panels 2, 3, and 4. It could be that the inner accretion disk empties itself to pump matter for the formation of the X-ray corona.

4.4. Is the Disk–Corona Relation Restored?

Although there is no consensus on the exact origin, geometry, and location of the AGN corona, there is substantial evidence that the accretion disk and the corona of AGNs are coupled to each other over a wide range of mass, luminosity, and accretion states, and this coupling is universal across all redshifts (Lusso et al. 2010; Lusso & Risaliti 2016). The universal coupling of the UV-emitting disk and corona suggests that the disk supplies the seed photons that the corona upscatters (inverse Comptonization), and we observe a power law at energies > 2 keV. The relation between the disk UV photons and the X-ray emission is measured by the correlation between α_{OX} and $L_{2500 \text{ \AA}}$, which is very tight even when considering local Seyferts and high-redshift luminous quasars (Laha et al. 2014b; Martocchia et al. 2017;

Laha et al. 2018, 2021). However, in the case of 1ES 1927 we do not detect any correlation between the UV and the X-ray photons during the violent event. The corona was disrupted much later (~ 200 days) than the first UV flare happened. The α_{OX} values during the flare are reported in Table 2. Figure 6 shows that in the pre-CL state (denoted by red star), the AGN was slightly below the disk–corona relation, but the relation was completely disrupted during the flare, with the parameter values spanning large regions in the phase space. However, as the source returned to the quiescent state (the blue triangles in the lower-left corner of Figure 6), the α_{OX} values (~ 1.02) returned back to their preflare values, indicating that the disk–corona link has again been established. The postflare values of α_{OX} and $L_{2500\text{ \AA}}$ lie on the correlation detected in AGN samples (Lusso et al. 2010; Lusso & Risaliti 2016).

4.5. Variability in the Narrow-line Region

In both the pre-CL and post-CL spectra we detect mostly narrow emission lines (see Tables 3 and 4). Except for the $\text{H}\beta$ emission line, we find that all the lines have evolved between 2011 and 2021. For example, new emission lines of $[\text{O II}]3727\text{ \AA}$, $\text{He II } 4686\text{ \AA}$, and $\text{O I } 6300\text{ \AA}$ emerged in the post-CL 2021 GTC spectra (see Table 4, last column). On the other hand, the $[\text{O III}]4959\text{ \AA}$ and $[\text{O III}]5007\text{ \AA}$ doublet became weaker in 2021. The $[\text{N II}]6548\text{ \AA}$ and $[\text{N II}]6584\text{ \AA}$ doublets became stronger. In addition, we also find a new emerging narrow He II emission line in 2021. If the narrow-line region is $\sim 1\text{--}10$ pc away from the central engine, any flux variations from the AGN would require $\sim 3\text{--}30$ yr to reach the NLR. Maybe we have just started to see the changes, given the fact that the 2021 observation was made ~ 3 yr after the start of the flare. Future monitoring is crucial to detect any further changes and thereby determine the distance and extent of the NLR.

4.6. The Nature of the Broad-line Region: Does True Type II Exist?

The missing BLR in the AGN 1ES 1927+654 throws a real challenge to unification theory. This source has been classified as a true Type II (Gallo et al. 2013), which we know now, may not be true, given the fact that we indeed detect a BLR during the high-flux state. The distance of the BLR ($\sim 100\text{--}150$ lt-days) is also of similar order to that predicted by reverberation mapping studies Peterson (1993). In our work, we detected a weak broad $\text{H}\alpha$ emission line with $\text{FWHM} \sim 2644 \pm 700\text{ km s}^{-1}$ in the 2011 TNG optical spectrum, indicating the presence of a BLR that is very weak. We note that this emission line may not arise from the same BLR region as detected by Trakhtenbrot et al. (2019), with $\text{FWHM} \sim 17,000\text{ km s}^{-1}$. Interestingly, we do not detect any such broad line in the post-CL 2021 GTC optical spectra. The detection of the weak broad $\text{H}\alpha$ emission line poses interesting challenges to our knowledge of true Type II sources. Perhaps the BLR always existed, it is just that it is not bright enough to be detected, given that the source is accreting at a very low rate.

For example, the nearby AGN NGC 3147 has been referred to as one of the best cases of a true Type II AGN, implying no absorption along the line of sight, yet there is no broad line present. However, for a low-luminosity AGN like NGC 3147 one would expect to have a broad line that is highly compact and hence hard to detect against the background host galaxy. Bianchi et al. (2019) carried out a narrow-slit ($0''.1 \times 0''.1$) Hubble Space Telescope (HST) spectroscopy for this source, which allowed them to exclude most of the host-galaxy light.

Very interestingly, they detected a broad $\text{H}\alpha$ emission line with a full width at zero intensity (FWZI) of $\sim 27,000\text{ km s}^{-1}$. This result challenges the very notion of “true Type II classification.” Coupling these with our results, we propose that there may not be any source that can be called a true Type II. Future narrow-slit spectroscopy of low accretion sources can reveal further information.

4.7. What is the Extended Radio Emission? Is There Any Evidence of Jet Formation?

Archival, or preflare, VLA observations of the source at 1.4 GHz (1995 NVSS; Condon et al. 1998), 5 GHz (1992), and 8 GHz (1998) show unresolved cores (\sim tens of parsecs to kiloparsecs) with a peak flux of 40, 16, and 9 mJy, respectively. This can be compared with VLBI preflare observations, where we see that the total flux is only one-quarter to one-half of these values, similar to the reductions in observed flux on arcsecond to milliarcsecond scales for radio-loud AGNs (e.g., Giovannini et al. 2005). The extended emission detected in VLBI imaging has very similar flux and shape through 2018 December and 2021 March. It is unclear if the absence of extended emission in the matching-resolution 2014 March epoch is intrinsic or mainly undetectable due to nonoptimal $u-v$ coverage and depth of the observation. The comparison of the NVSS and EVN fluxes at 1.5 GHz do suggest extended emission is present, but the resolution of NVSS is very poor ($45''$), and we also see discrepancies between the total VLBI-scale flux in 2018/2021 and the corresponding VLA observations. Whether this is due to variability or additional extended emission beyond the VLBI scale, we cannot say.

Extended radio emission from RQ AGNs may arise in different ways (see e.g., Panessa et al. 2019 for a recent review), with the spatial extent being an important clue. If it is on the scale of the galaxy, it may be attributed to star formation, which is verifiable with far-IR observations. If the structure is small enough and not resolved with the VLA, but resolved on the milliarcsecond scale, it could be a nascent jet, as was recently discovered in the CL-AGN Mkn 590 Yang et al. (2021). In the case of 1ES 1927, the best-fit model is an extended uniformly illuminated disk and the emission is seemingly isotropic. This is contrary to the general picture of jets from black holes, which are usually highly collimated. An extended disk wind that is bright due to free-free emission may also be a possibility (Panessa et al. 2019), but we need higher-frequency observations and better constraints on the spectral slope to verify this. Further, naively using the approximate disk size of 5 lt-yr and assuming it grew to this size in ~ 1 yr from the onset of optical-UV flaring due to the TDE, the apparent speed $\gtrsim 2c$. This is obviously problematic for either a collimated outflow (which our observations do not resemble) or a subrelativistic disk wind, or essentially any origin that is novel since the CL event. The extended emission may also possibly represent the outskirts of a maser disk, as found in NGC 1068 or NGC 4258 (e.g., Greenhill et al. 1995; Gallimore et al. 2004), which can only be verified through deep spectroscopic studies.

5. Conclusions

In this work we report the evolution of the radio, optical, UV, and X-rays from the preflare state through mid-2021 with new and archival data from the Very Long Baseline Array, the Very Large Array, the Telescopio Nazionale Galileo, Gran Telescopio Canarias, The Neil Gehrels Swift observatory, and XMM-Newton. The main results from our work are:

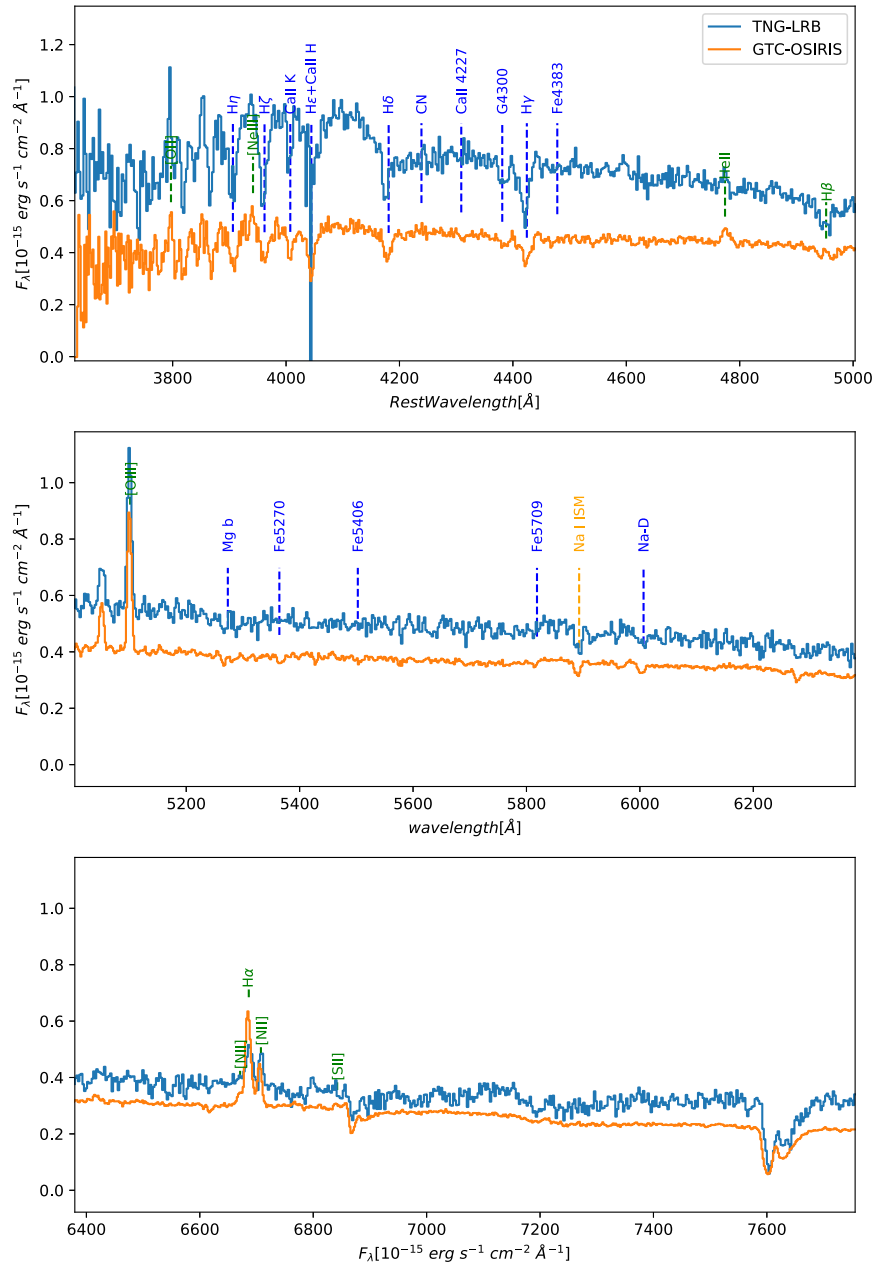


Figure A2. The comparison between the pre-CL and post-CL optical spectra. The blue spectrum is the 2011 TNG observation, while the orange one is from 2021 GTC observations. The 2011 spectrum is much bluer than the 2021 one.

feature to be measured. The line center is estimated as the mass center, the flux by adding the emission within the line interval, and the EW as the flux divided by the continuum at the line center. Most of the emission lines seem to have compatible values for the flux and EWs within 2σ . The only exceptions are the complex $H\alpha + [N II]$, which shows a larger emission flux in the 2021 spectrum. Despite the difficulties measuring the absorption features in the TNG/LRB spectrum due to the low signal-to-noise ratio in the blue part, the EWs of absorption features are compatible between the two epochs, specially the Balmer lines $H\delta$ and $H\gamma$. The exception is the line $H\beta$, which shows a smaller EW in the 2021 spectrum. This is compatible with a deeper absorption contribution (in absorbed flux but not in EW) or alternatively an

increase in the emission contribution (the $H\beta$ profile is formed by the contributions of the stellar absorption and the emission one). Later, after modeling stellar population emission, one could discern which scenario is favored. High-order Balmer lines are more dominated by the stellar emission and low order $H\alpha$ and $H\beta$ are more contaminated by the emission from the ionized gas of the NLR. From this comparison, it can be said that the stellar emission seems to be compatible in the spectra taken in the two epochs, 2011 and 2021, despite the difference in flux which can be due to the different aperture used. In Figure A1 we show the two GTC spectra obtained in 2021 March and May. In Figure A2 we show the comparison between the two spectra at the two epochs: 2011 TNG and 2021 GTC.

A.1.2. Zooming into the Balmer Emission-line Profiles

In Figures A3 and A4, we show the zoomed-in data+model+residuals of the H α and H β complex. We did not detect any broad emission line consistent with that observed by Trakhtenbrot et al. (2019). See Section 2.3.3 for details.

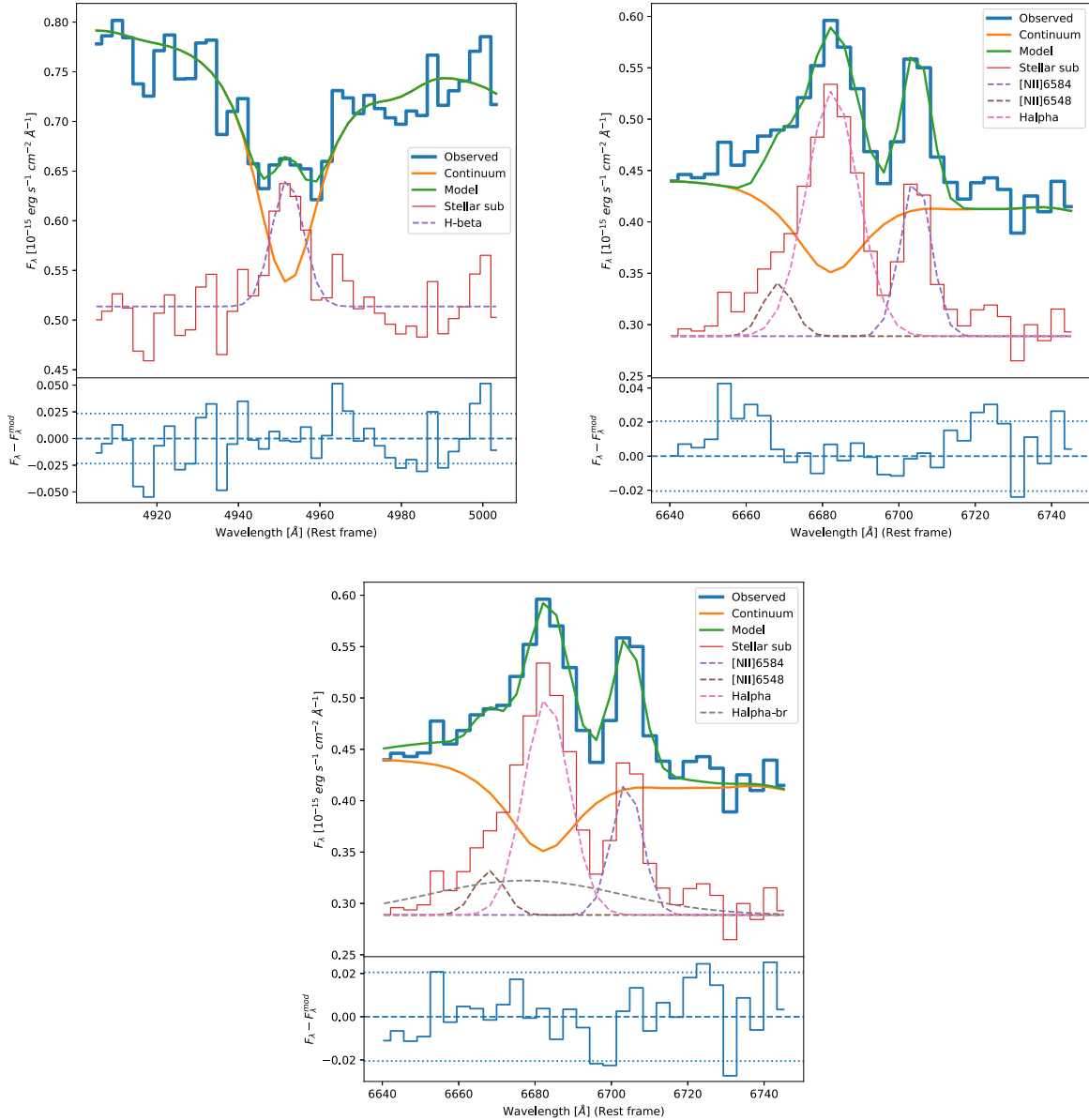


Figure A3. The 2011 TNG Optical spectrum of 1ES 1927+654 zooming in the crucial H β and H α regions. For all the panels, the stellar model and the emission-line fits are shown. The residuals compared to the full model, including the stellar model plus the emission-line fits, are plotted in the bottom panel of each figure. Top left: the H β line detected in absorption in the observed spectrum and in emission after correcting for the host stellar absorption. Top right: same as left figure, but for the H α emission-line complex. Bottom: same as the top-right figure, but after fitting with a broad Gaussian to model the broad H α emission line.

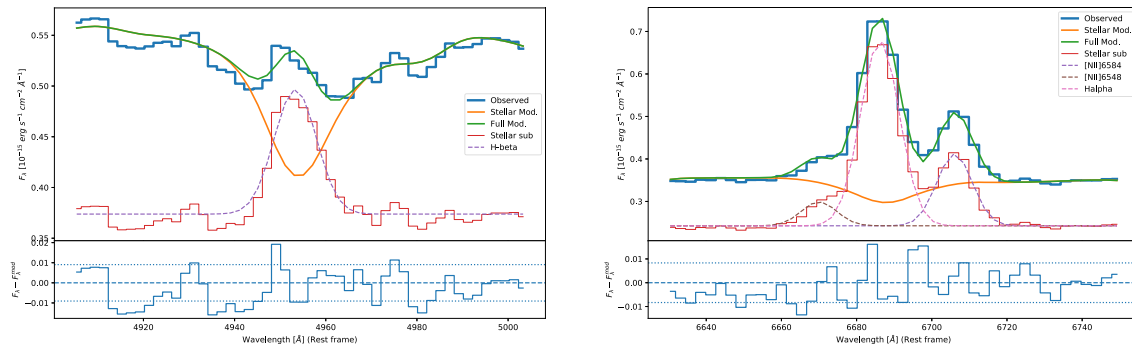


Figure A4. The 2021 GTC optical spectrum of 1ES 1927+654 zooming in the crucial H β and H α regions. The stellar model and the emission-line fits are shown in the top panel of each of the two figures. The residuals compared to the full model, including the stellar model plus the emission-line fits, are plotted in the bottom panel. We do not detect any broad emission line in the 2021 spectra.

ORCID iDs

Sibasish Laha <https://orcid.org/0000-0003-2714-0487>
 Eileen Meyer <https://orcid.org/0000-0002-7676-9962>
 Agniva Roychowdhury <https://orcid.org/0000-0003-1101-8436>
 Josefa Becerra Gonzalez <https://orcid.org/0000-0002-6729-9022>
 J. A. Acosta-Pulido <https://orcid.org/0000-0002-0433-9656>
 Aditya Thapa <https://orcid.org/0000-0002-8843-9581>
 Ritesh Ghosh <https://orcid.org/0000-0003-4790-2653>
 Ehud Behar <https://orcid.org/0000-0001-9735-4873>
 Gerard A. Kriss <https://orcid.org/0000-0002-2180-8266>
 Francesca Panessa <https://orcid.org/0000-0003-0543-3617>
 Stefano Bianchi <https://orcid.org/0000-0002-4622-4240>
 Fabio La Franca <https://orcid.org/0000-0002-1239-2721>
 Mitchell C. Begelman <https://orcid.org/0000-0003-0936-8488>
 Anna Lia Longinotti <https://orcid.org/0000-0001-8825-3624>
 Elisabeta Lusso <https://orcid.org/0000-0003-0083-1157>
 Samantha Oates <https://orcid.org/0000-0001-9309-7873>
 Matt Nicholl <https://orcid.org/0000-0002-2555-3192>
 S. Bradley Cenko <https://orcid.org/0000-0003-1673-970X>

References

- Barvainis, R., Lehár, J., Birkinshaw, M., Falcke, H., & Blundell, K. M. 2005, *ApJ*, 618, 108
- Bianchi, S., Panessa, F., Barcons, X., et al. 2012, *MNRAS*, 426, 3225
- Bianchi, S., Antonucci, R., Capetti, A., et al. 2019, *MNRAS*, 488, L1
- Boller, T., Voges, W., Dennefeld, M., et al. 2003, *A&A*, 397, 557
- Breeveld, A. A., Landsman, W., Holland, S. T., et al. 2011, in AIP Conf. Ser. 1358, *Gamma Ray Bursts 2010*, ed. J. E. McEnery, J. L. Racusin, & N. Gehrels (Melville, NY: AIP), 373
- Briggs, D. S. 1995, AAS Meeting Abstracts, 187, 112.02
- Burrows, D. N., Hill, J. E., Nousek, J. A., et al. 2005, *SSRv*, 120, 165
- Cappellari, M. 2017, *MNRAS*, 466, 798
- Cappellari, M., & Emsellem, E. 2004, *PASP*, 116, 138
- Chael, A. A., Johnson, M. D., Bouman, K. L., et al. 2018, *ApJ*, 857, 23
- Chan, C.-H., Piran, T., Krolik, J. H., & Saban, D. 2019, *ApJ*, 881, 113
- Cohen, R. D., Rudy, R. J., Puetter, R. C., Ake, T. B., & Foltz, C. B. 1986, *ApJ*, 311, 135
- Condon, J. J., Cotton, W. D., Greisen, E. W., et al. 1998, *aj*, 115, 1693
- Denney, K. D., De Rosa, G., Croxall, K., et al. 2014, *ApJ*, 796, 134
- Dexter, J., McKinney, J. C., Markoff, S., & Tchekhovskoy, A. 2014, *MNRAS*, 440, 2185
- Done, C., Davis, S. W., Jin, C., Blaes, O., & Ward, M. 2012, *MNRAS*, 420, 1848
- Ehler, H. J. S., Gonzalez, A. G., & Gallo, L. C. 2018, *MNRAS*, 478, 4214
- Fitzpatrick, E. L. 1999, *PASP*, 111, 63
- Gallimore, J. F., Baum, S. A., & O'Dea, C. P. 2004, *ApJ*, 613, 794
- Gallo, L. C., Blue, D. M., Grupe, D., Komossa, S., & Wilkins, D. R. 2018, *MNRAS*, 478, 2557
- Gallo, L. C., MacMackin, C., Vasudevan, R., et al. 2013, *MNRAS*, 433, 421
- Gallo, L. C., Gonzalez, A. G., Waddell, S. G. H., et al. 2019, *MNRAS*, 484, 4287
- García, J., Dauser, T., Lohfink, A., et al. 2014, *ApJ*, 782, 76
- García, J. A., Kara, E., Walton, D., et al. 2019, *ApJ*, 871, 88
- Güdel, M., & Benz, A. O. 1993, *ApJ*, 405, L63
- Ghosh, R., & Laha, S. 2020, *MNRAS*, 497, 4213
- Giovannini, G., Taylor, G. B., Ferretti, L., et al. 2005, *ApJ*, 618, 635
- Greenhill, L. J., Jiang, D. R., Moran, J. M., et al. 1995, *ApJ*, 440, 619
- Grupe, D., Komossa, S., Gallo, L. C., et al. 2012, *ApJS*, 199, 28
- Husemann, B., Urrutia, T., Tremblay, G. R., et al. 2016, *A&A*, 593, L9
- Jansen, F., Lumb, D., Altieri, B., et al. 2001, *A&A*, 365, L1
- Janssen, M., Goddi, C., van Bommel, I. M., et al. 2019, *A&A*, 626, A75
- Kara, E., Alston, W. N., Fabian, A. C., et al. 2016, *MNRAS*, 462, 511
- Kara, E., Steiner, J. F., Fabian, A. C., et al. 2019, *Nat*, 565, 198
- Kewley, L. J., Groves, B., Kauffmann, G., & Heckman, T. 2006, *MNRAS*, 372, 961
- Laha, S., Dewangan, G. C., Chakravorty, S., & Kembhavi, A. K. 2013, *ApJ*, 777, 2
- Laha, S., Dewangan, G. C., & Kembhavi, A. K. 2011, *ApJ*, 734, 75
- Laha, S., Dewangan, G. C., & Kembhavi, A. K. 2014a, *MNRAS*, 437, 2664
- Laha, S., & Ghosh, R. 2021, *ApJ*, 915, 93
- Laha, S., Ghosh, R., Guainazzi, M., & Markowitz, A. G. 2018, *MNRAS*, 480, 1522
- Laha, S., Ghosh, R., Tripathi, S., & Guainazzi, M. 2019, *MNRAS*, 486, 3124
- Laha, S., Guainazzi, M., Dewangan, G. C., Chakravorty, S., & Kembhavi, A. K. 2014b, *MNRAS*, 441, 2613
- Laha, S., Markowitz, A. G., Krumpel, M., et al. 2020, *ApJ*, 897, 66
- Laha, S., Reynolds, C. S., Reeves, J., et al. 2021, *NatAs*, 5, 13
- LaMassa, S. M., Cales, S., Moran, E. C., et al. 2015, *ApJ*, 800, 144
- Laor, A., & Behar, E. 2008, *MNRAS*, 390, 847
- Lusso, E., & Risaliti, G. 2016, *ApJ*, 819, 154
- Lusso, E., Comastri, A., Vignali, C., et al. 2010, *A&A*, 512, A34
- Marconi, A., Risaliti, G., Gilli, R., et al. 2004, *MNRAS*, 351, 169
- Martocchia, S., Piconcelli, E., Zappacosta, L., et al. 2017, *A&A*, 608, A51
- Mason, K. O., Breeveld, A., Much, R., et al. 2001, *A&A*, 365, L36
- Mathur, S., Denney, K. D., Gupta, A., et al. 2018, *ApJ*, 866, 123
- McMullin, J. P., Waters, B., Schiebel, D., Young, W., & Golap, K. 2007, in ASP Conf. Ser. 376, *Astronomical Data Analysis Software and Systems XVI*, ed. R. A. Shaw, F. Hill, & D. J. Bell (San Francisco, CA: ASP), 127
- Mundell, C. G., Ferruit, P., Nagar, N., & Wilson, A. S. 2009, *ApJ*, 703, 802
- Panessa, F., Baldi, R. D., Laor, A., et al. 2019, *NatAs*, 3, 387
- Panessa, F., & Bassani, L. 2002, *A&A*, 394, 435
- Panessa, F., Pérez-Torres, M., Hernández-García, L., et al. 2022, *MNRAS*, 510, 718
- Parker, M. L., Schartel, N., Grupe, D., et al. 2019, *MNRAS*, 483, L88
- Perlman, E. S., Stocke, J. T., Schachter, J. F., et al. 1996, *ApJS*, 104, 251
- Peterson, B. M. 1993, *PASP*, 105, 247
- Ricci, C., Kara, E., Loewenstein, M., et al. 2020, *ApJ*, 898, L1
- Ricci, C., Loewenstein, M., Kara, E., et al. 2021, *ApJS*, 255, 7
- Roming, P. W. A., Kennedy, T. E., Mason, K. O., et al. 2005, *SSRv*, 120, 95
- Scepi, N., Begelman, M. C., & Dexter, J. 2021, *MNRAS*, 502, L50
- Schawinski, K., Koss, M., Berney, S., & Sartori, L. F. 2015, *MNRAS*, 451, 2517
- Shepherd, M. C., Pearson, T. J., & Taylor, G. B. 1994, *BAAS*, 26, 987

- Strüder, L., Briel, U., Dennerl, K., et al. 2001, *A&A*, 365, L18
- Trakhtenbrot, B., Arcavi, I., MacLeod, C. L., et al. 2019, *ApJ*, 883, 94
- Tran, H. D., Lyke, J. E., & Mader, J. A. 2011, *ApJ*, 726, L21
- Tripathi, S., McGrath, K. M., Gallo, L. C., et al. 2020, *MNRAS*, 499, 1266
- Tripathi, S., Waddell, S. G. H., Gallo, L. C., Welsh, W. F., & Chiang, C. Y. 2019, *MNRAS*, 488, 4831
- Turner, M. J. L., Abbey, A., Arnaud, M., et al. 2001, *A&A*, 365, L27
- Ursini, F., Petrucci, P. O., Bianchi, S., et al. 2020, *A&A*, 634, A92
- van Velzen, S., Gezari, S., Hammerstein, E., et al. 2021, *ApJ*, 908, 4
- Vazdekis, A., Sánchez-Blázquez, P., Falcón-Barroso, J., et al. 2010, *MNRAS*, 404, 1639
- Waddell, S. G. H., Gallo, L. C., Gonzalez, A. G., Tripathi, S., & Zoghbi, A. 2019, *MNRAS*, 489, 5398
- Wang, J.-M., Du, P., Baldwin, J. A., et al. 2012, *ApJ*, 746, 137
- Wilkins, D. R., & Gallo, L. C. 2015, *MNRAS*, 449, 129
- Wilkins, D. R., Gallo, L. C., Grupe, D., et al. 2015, *MNRAS*, 454, 4440
- Yang, J., van Bemmell, I., Paragi, Z., et al. 2021, *MNRAS*, 502, L61
- Zetzl, M., Kollatschny, W., Ochmann, M. W., et al. 2018, *A&A*, 618, A83